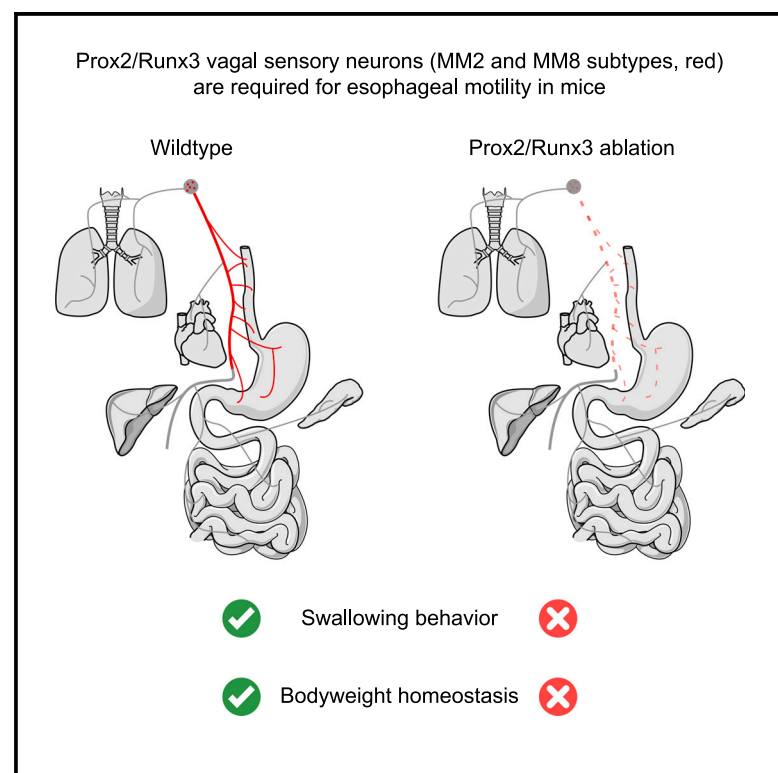


Prox2 and Runx3 vagal sensory neurons regulate esophageal motility

Graphical abstract



Authors

Elijah D. Lowenstein,
Pierre-Louis Ruffault,
Aristotelis Misios, ...,
Nikolaus Rajewsky, Teresa E. Lever,
Carmen Birchmeier

Correspondence

cbirch@mdc-berlin.de

In brief

The vagal sensory neurons that monitor esophageal stretch and distension belong to the MM2 and MM8 subtypes of Prox2/Runx3 neurons. These two subtypes are key for swallowing *in vivo*, as their ablation causes severe esophageal dysmotility. Knowledge about their molecular makeup might help treat esophageal disease.

Highlights

- Prox2/Runx3 vagal sensory neurons form intraganglionic laminar endings in the esophagus
- Prox2/Runx3 vagal sensory neurons function as mechanoreceptors
- Prox2/Runx3 vagal sensory neurons are required for swallowing in freely behaving mice



Article

Prox2 and Runx3 vagal sensory neurons regulate esophageal motility

Elijah D. Lowenstein,^{1,2} Pierre-Louis Ruffault,¹ Aristotelis Misios,^{1,2,3} Kate L. Osman,⁴ Huimin Li,⁵ Rachel S. Greenberg,⁶ Rebecca Thompson,⁴ Kun Song,¹ Stephan Dietrich,⁷ Xun Li,⁸ Nikita Vladimirov,⁹ Andrew Woehler,⁹ Jean-François Brunet,¹⁰ Niccolò Zampieri,⁷ Ralf Kühn,¹¹ Stephen D. Liberles,⁶ Shiqi Jia,⁵ Gary R. Lewin,¹² Nikolaus Rajewsky,³ Teresa E. Lever,⁴ and Carmen Birchmeier^{1,2,13,*}

¹Developmental Biology/Signal Transduction, Max Delbrück Center for Molecular Medicine, Berlin, Germany

²NeuroCure Cluster of Excellence, CharitéUniversitätsmedizin Berlin, Corporate Member of Freie Universität Berlin and Humboldt-Universität zu Berlin, Berlin, Germany

³Systems Biology of Gene Regulatory Elements, Berlin Institute for Medical Systems Biology, Max Delbrück Center for Molecular Medicine, Berlin, Germany

⁴Department of Otolaryngology - Head & Neck Surgery, University of Missouri School of Medicine, Columbia, MO, USA

⁵The First Affiliated Hospital, Jinan University, Guangzhou, China

⁶Howard Hughes Medical Institute, Department of Cell Biology, Harvard Medical School, Boston, MA 02115, USA

⁷Development and Function of Neural Circuits, Max Delbrück Center for Molecular Medicine, Berlin, Germany

⁸Immune Regulation and Cancer, Max Delbrück Center for Molecular Medicine, Berlin, Germany

⁹Systems Biology Imaging, Berlin Institute for Medical Systems Biology, Max Delbrück Center for Molecular Medicine, Berlin, Germany

¹⁰Institut de Biologie de l'ENS (IBENS), Inserm, CNRS, École normale supérieure, PSL Research University, Paris, France

¹¹Genome Engineering & Disease Models, Max Delbrück Center for Molecular Medicine, Berlin, Germany

¹²Molecular Physiology of Somatic Sensation, Max Delbrück Center for Molecular Medicine, Berlin, Germany

¹³Lead contact

*Correspondence: cbirch@mdc-berlin.de

<https://doi.org/10.1016/j.neuron.2023.04.025>

SUMMARY

Vagal sensory neurons monitor mechanical and chemical stimuli in the gastrointestinal tract. Major efforts are underway to assign physiological functions to the many distinct subtypes of vagal sensory neurons. Here, we use genetically guided anatomical tracing, optogenetics, and electrophysiology to identify and characterize vagal sensory neuron subtypes expressing *Prox2* and *Runx3* in mice. We show that three of these neuronal subtypes innervate the esophagus and stomach in regionalized patterns, where they form intraganglionic laminar endings. Electrophysiological analysis revealed that they are low-threshold mechanoreceptors but possess different adaptation properties. Lastly, genetic ablation of *Prox2* and *Runx3* neurons demonstrated their essential roles for esophageal peristalsis in freely behaving mice. Our work defines the identity and function of the vagal neurons that provide mechanosensory feedback from the esophagus to the brain and could lead to better understanding and treatment of esophageal motility disorders.

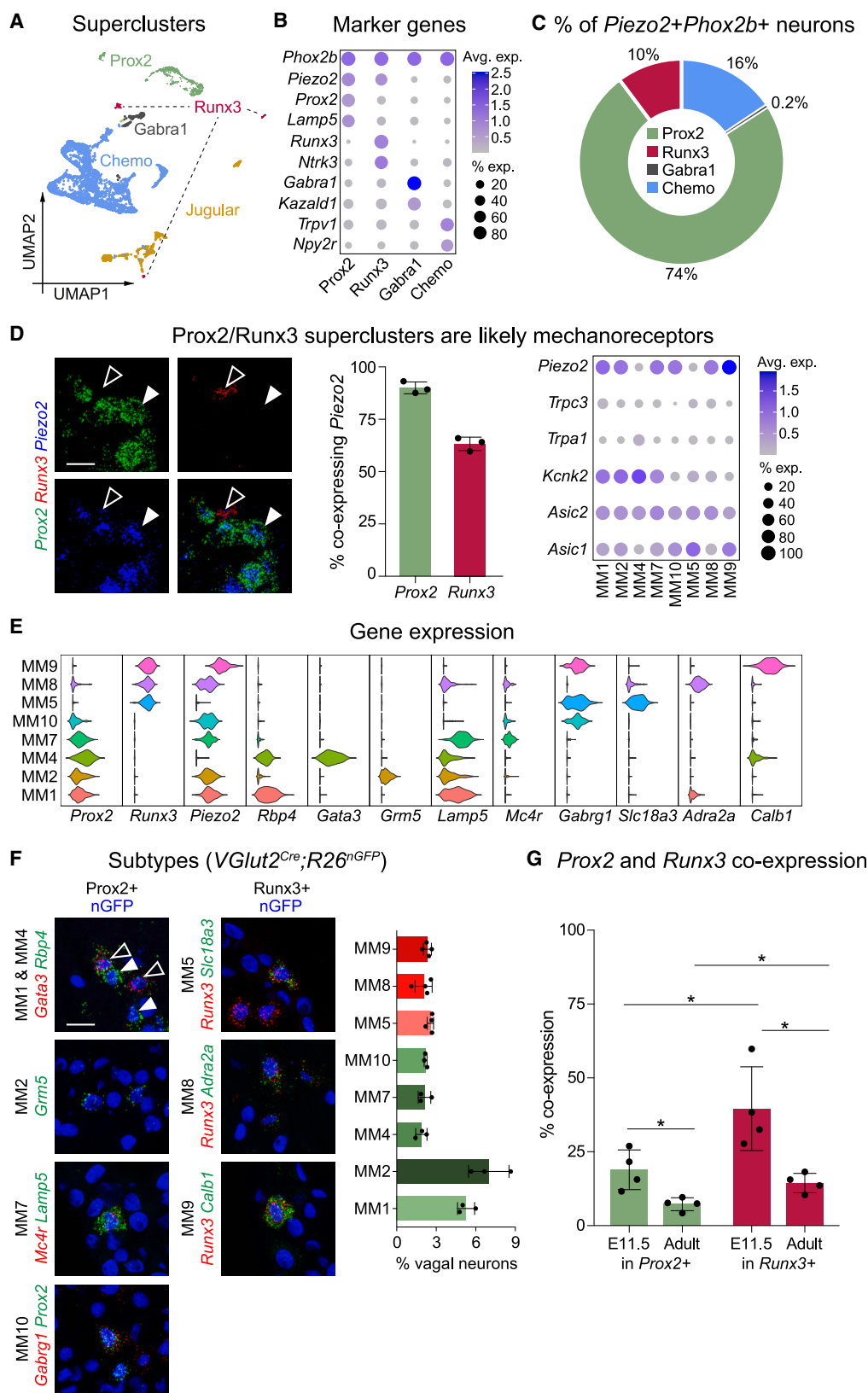
INTRODUCTION

Sensory signaling through the vagus nerve relays vital information from internal organs to the brain and controls various aspects of bodily homeostasis.^{1,2} During food intake and digestion, the ingested bolus exerts mechanical force against the walls of the digestive tract. Nodose (also called inferior vagal ganglion) sensory neurons detect stretch and tension in the digestive tract and transmit information on the location and size of the bolus to the brain.³ This triggers the physiological and behavioral responses needed for food intake, such as gut motility and appetite control.⁴

Several types of mechanosensory neurons displaying distinct electrophysiological properties and endings, like intraganglionic laminar endings (IGLEs), intramuscular arrays (IMAs), and

mucosal endings, have been defined in the gastrointestinal tract by electrophysiological and histological techniques.^{5–9} Due to the vast heterogeneity of vagal sensory neurons, their molecular characteristics were only recently defined using single-cell RNA sequencing (scRNA-seq).^{10–12} Further, work over the past few years has begun to characterize the properties of some of the neuronal subtypes important for digestion, using molecular and genetic tools. For example, two vagal subtypes forming IGLEs that contact intestinal and stomach enteric ganglia express *Oxtr* and *Glp1r*, respectively, and *Glp1r*+ stomach IGLEs were shown to detect stretch.^{10,13} Further, recent work assigned *Piezo2*+*Grm5*+*Slit2*+ neurons as esophageal IMAs that respond to stretch.¹⁴ Vagal IGLEs also innervate esophageal enteric ganglia,⁶ but their molecular signature and function is unknown.





(legend on next page)

Swallowing is an active process that transports food and liquid from the mouth to the stomach via the esophagus. The esophageal phase of swallowing requires peristaltic movements of the esophageal wall, which are controlled by reflexes executed by vagal motor nuclei in the hindbrain (dorsal motor nucleus of the vagus [DMV] and nucleus ambiguus [NA]), and esophageal enteric ganglia.^{15–17} Esophageal motility disorders are characterized by dysphagia and are frequent comorbidities of aging and age-related neurological disease.^{18–20} The etiology underlying dysphagia is mostly unknown, which is also due to the lack of knowledge about the sensorimotor circuits involved.²¹ The first studies of esophageal physiology were undertaken in the late 19th century, and for the following decades it was debated whether the activity of hindbrain swallowing centers (hindbrain vagal motor nuclei and the nucleus of the solitary tract [NTS]) suffices to generate esophageal peristalsis, or whether vagal sensory feedback is also required.^{22–24} Several lines of evidence suggested a role for peripheral feedback in esophageal function.^{25–27} Classical studies often relied on blunt transection of the vagus nerve and therefore affected both sensory and motor fibers. Furthermore, they were often performed under anesthesia, which affects esophageal peristalsis.²⁶ Swallowing in awake, freely behaving rodents can be observed using video-fluoroscopic swallowing studies (VFSSs).^{28–30} Thus, ablation of specific vagal sensory neurons that innervate the esophagus combined with VFSS can conclusively demonstrate the role of sensory feedback in esophageal peristalsis.

Here, we used scRNA-seq to characterize vagal mechanosensory neuronal heterogeneity, and identified subtype specific markers useful for genetic analysis. We found that two transcription factors, *Prox2* and *Runx3*, define the majority of nodose neurons expressing the mechanosensitive ion channel, *Piezo2*, and provide evidence that neurons expressing *Prox2* and *Runx3* are developmentally related. We refer to neurons expressing either *Prox2* or *Runx3* as *Prox2/Runx3* neurons and show that they encompass eight neuronal subtypes. Genetically guided neuronal tracing and anatomical analyses demonstrated that three *Prox2/Runx3* vagal neuronal subtypes innervate the esophagus and stomach, where they form IGLs on enteric ganglia. Electrophysiological and optogenetic analyses demonstrated that these three *Prox2/Runx3* subtypes are low-threshold mechanoreceptors. Lastly, we ablated *Prox2/Runx3* neurons using intersectional genetic tools and performed VFSS in awake and unrestrained animals, revealing that these neurons are required for esophageal motility. Our data demonstrate the existence of specific vagal neuron subtypes controlling esopha-

geal peristalsis and body homeostasis by relaying mechanosensory information from the esophagus to the brain.

RESULTS

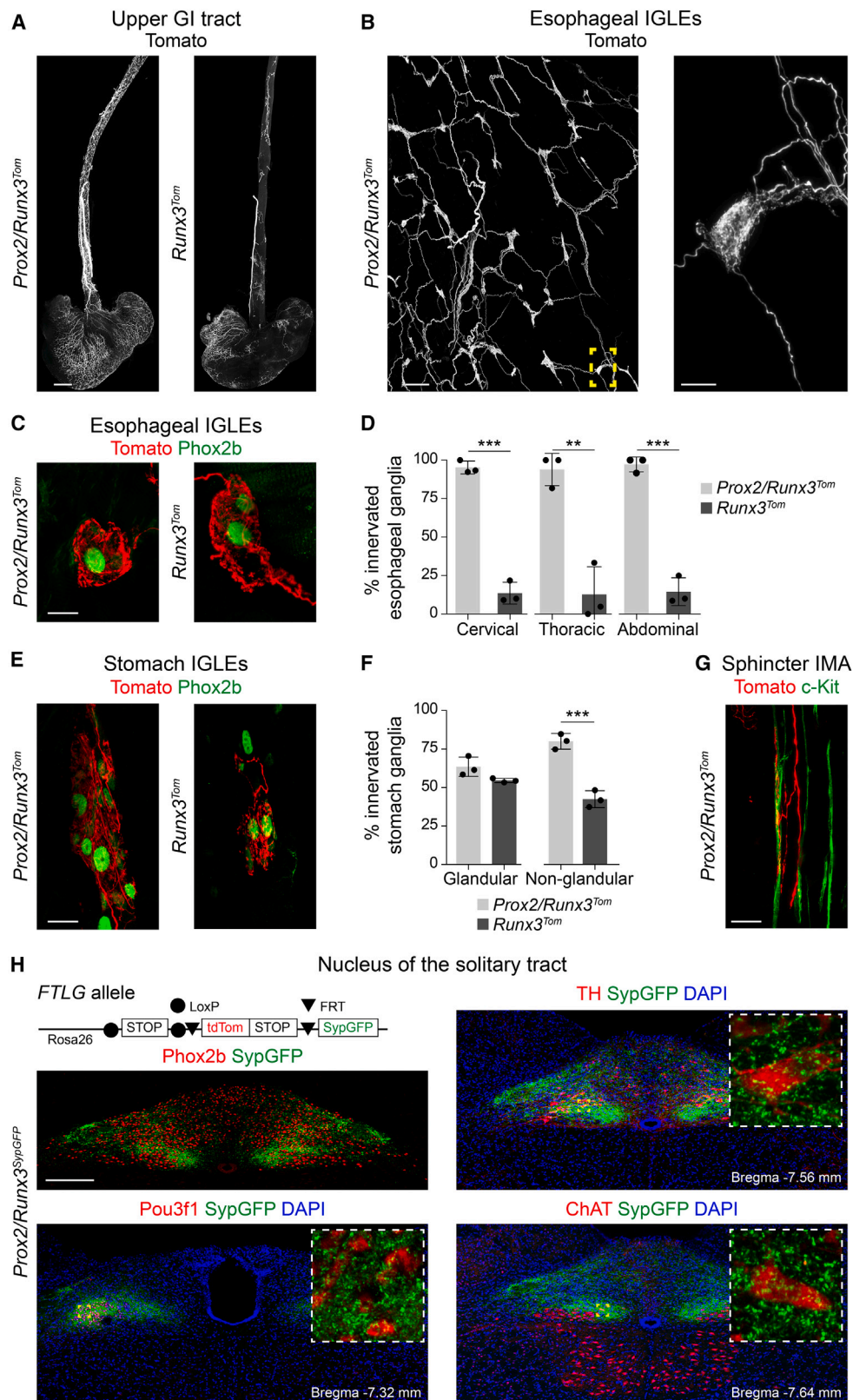
Molecular characterization of vagal mechanosensory neurons

To perform scRNA-seq, we isolated vagal sensory neurons using flow cytometry after genetically labeling all vagal neurons with a nuclear GFP (nGFP) reporter (ganglia from 15 *VGlut2^{Cre};R26^{nGFP}* mice at postnatal day [P] 4, Figure S1A). We used Cell Expression by Linear amplification and Sequencing-2 (CEL-Seq2), a low-throughput method with high gene detection sensitivity, and sequenced 1,536 cells.^{31,32} After removing cells with more than 250,000 or less than 17,000 unique molecular identifiers (UMIs), 1,392 cells remained for which a median of 9,323 genes and 70,667 UMIs were identified. Bioinformatic analysis defined 22 distinct neuronal subtypes (Figure S1B). We integrated our data with two scRNA-seq datasets of vagal neurons published during this study to perform a meta-analysis on 4,442 vagal neurons, i.e., 1,392 neurons isolated at P4 (this study), 395 and 956 neurons isolated at P42 and P56–84, respectively,¹⁰ and 1,707 neurons isolated between P32 and 35.¹¹ Uniform manifold approximation and projection (UMAP) analysis of the combined datasets improved the resolution of vagal neuron types and segregated the roughly 10,000 vagal neurons per mouse into 27 transcriptomically distinct subtypes (Figure S1C). Cells from all datasets contributed to all 27 subtypes, indicating that shortly after birth all subtypes are specified (Figure S1D). The meta-analysis can be explored at <https://shiny.mdc-berlin.de/VGIE/>.

A semi-supervised method was applied to group the 27 vagal neuron subtypes into “superclusters” (Figure 1A). The superclusters distinguish the two parts of the vagal ganglion, the nodose and jugular ganglion, which derive from the epibranchial placode and cranial neural crest, respectively.^{33,34} Whereas nodose neurons control the function of inner organs, jugular neurons allow somatic sensation and resemble dorsal root ganglia (DRG) neurons. Nodose and jugular neurons express *Phox2b* and *Prrxl1*, respectively (Figures S1E and S1G).^{35,36} Nodose neurons could be subdivided into four superclusters: “*Prox2*,” expressing the homeobox transcription factor *Prox2*; “*Gabra1*,” expressing the $\alpha 1$ subunit of the γ -aminobutyric acid type A (GABAA) receptor; “*Chemo*,” a putative chemoreceptor supercluster expressing *Trpv1* and *Npy2r*; and “*Runx3*,” expressing the runt-related transcription factor *Runx3* (Figures 1A and 1B); the latter supercluster arose by merging three small subtypes scattered in the UMAP.

Figure 1. Meta-analysis of vagal neurons identified the *Prox2* and *Runx3* superclusters of putative mechanoreceptors

- (A) UMAP plot based on a meta-analysis of scRNA-seq data from this work and two published reports,^{10,11} showing five superclusters (*Prox2*, *Runx3*, *Gabra1*, *Chemo*, *Jugular*).
- (B) Dot plot of selected genes that define four *Phox2b*+ superclusters (*Prox2*, *Runx3*, *Gabra1*, *Chemo*).
- (C) Donut chart showing the supercluster identity of *Piezo2*+*Phox2b*+ neurons.
- (D) Left, smFISH for *Prox2* (green), *Runx3* (red), and *Piezo2* (blue) mRNA on vagal ganglia sections from wild-type mice at P8. Middle, quantification of *Prox2*+ and *Runx3*+ neurons co-expressing *Piezo2*; n = 3. Scale bar, 20 μ m. Right, dot plot showing expression of selected genes implicated in mechanosensation in *Prox2/Runx3* subtypes.
- (E) Violin plots of genes used to identify the *Prox2/Runx3* subtypes in (F).
- (F) Left, smFISH images of *Prox2*+ subtypes. Middle, smFISH images of *Runx3*+ subtypes. smFISH was performed on vagal ganglia of *VGlut2^{Cre};R26^{nGFP}* mice at P8; neuronal nuclei expressing nGFP are shown in blue. Scale bar, 20 μ m. Right, quantifications of *Prox2*+ and *Runx3*+ subtypes; n = 3–4.
- (G) Quantification of *Prox2* and *Runx3* co-expression; n = 4. Data are represented as mean \pm SD, *p < 0.05, unpaired two-tailed t test. See also Figure S1.



(legend on next page)

Around 84% of all nodose *Phox2b*+*Piezo2*+ neurons were assigned to the *Prox2* and *Runx3* superclusters, which was verified by single-molecule fluorescence *in situ* hybridization (smFISH) (Figures 1C, 1D, S1F, and S1G). As *Piezo2* transduces mechanical information in many neuron types,^{37,38} we hypothesized that the *Prox2* and *Runx3* superclusters were candidate mechanoreceptors. In accordance, *Prox2* and *Runx3* neuronal subtypes express additional genes implicated in mechanoreception, like *Kcnk2*, *Asic1/2*, *Trpc3*, and *Trpa1* (Figure 1D).³⁹ The remaining nodose *Phox2b*+*Piezo2*+ neurons were assigned to the Chemo supercluster and might correspond to polymodal afferents (Figure 1C).

The *Prox2* and *Runx3* superclusters encompass five and three transcriptomically unique neuronal subtypes, respectively; we refer to them as meta-analysis putative mechanoreceptors MM1, MM2, MM4, MM7, MM10 (*Prox2*-positive) and MM5, MM8, MM9 (*Runx3*-positive). Four and two of the *Prox2* and *Runx3* subtypes, respectively, express *Piezo2*. Each subtype is defined by the expression of specific marker genes, which was verified on vagal ganglia sections using smFISH, and each subtype represents 2%–8% of all vagal neurons (Figures 1E and 1F). In the adult mouse, the majority of *Prox2* and *Runx3* neurons exclusively expressed one of these two transcription factors, although *Prox2* and *Runx3* were extensively co-expressed during development. In particular, 39.6% ± 14.2% of *Runx3*+ neurons co-expressed *Prox2* at E11.5, suggesting that *Prox2* and *Runx3* neurons are developmentally related (Figure 1G).

Generation of genetic tools for the analysis of *Prox2* and *Runx3* neurons

We generated a *Prox2*^{FlpO} knockin mouse strain to investigate putative vagal mechanoreceptors (Figure S2A). Work done in chickens and mice demonstrated that *Prox2* expression is restricted to subsets of neurons in placodally derived cranial ganglia during development (Figure S2B).^{40–44} Further, *Prox2* is also expressed in non-neuronal cells such as sperm and possibly the lens.⁴⁰ We used an intersectional genetic strategy combining *Prox2*^{FlpO} and *Phox2b*^{Cre} with *Ai65*, a reporter allele that expresses cytoplasmic tdTomato fluorescent protein after Cre- and Flp-mediated recombination, to label vagal sensory neurons. We observed recombination in both *Prox2*+ and *Runx3*+ vagal sensory neurons, which reflected their shared developmental history (Figure 1G). 94.8% ± 3.6% and

71.4% ± 2.1% of vagal *Prox2*+ and *Runx3*+ neurons, including all eight *Prox2*/*Runx3* subtypes, were recombined (Figures S2C–S2E). As *Prox2*^{FlpO};*Phox2b*^{Cre};*Ai65* mice recombine both *Prox2*+ and *Runx3*+ vagal subtypes, we hereafter refer to these animals as *Prox2*/*Runx3*^{Tom} (Figures S2F and S2G).

To distinguish between *Prox2* and *Runx3* neuronal projection patterns, we used the *Runx3*^{Cre} allele.⁴⁵ *Runx3* is expressed in subpopulations of nodose neurons, DRG proprioceptive neurons, and various non-neuronal cell types.^{46,47} To label vagal *Runx3*+ neurons, we initially analyzed *Runx3*^{Cre};*Phox2b*^{FlpO};*Ai65* mice. Although vagal *Runx3*+ neurons were recombined, we observed variable recombination in enteric and sympathetic ganglia (data not shown). Therefore, we used a distinct intersectional approach, *Runx3*^{Cre};*Prox2*^{FlpO};*Ai65* animals, which recombined 70.5% ± 4.8% of vagal *Runx3*+ neurons and all *Runx3*+ neuron subtypes, but only a minor proportion of *Prox2*+ neurons (Figures S2C–S2E). As *Runx3*^{Cre};*Prox2*^{FlpO};*Ai65* mice only recombined *Runx3* vagal subtypes, we hereafter refer to these animals as *Runx3*^{Tom} (Figures S2D and S2H).

Next, we searched for additional recombination sites in *Prox2*/*Runx3*^{Tom} and *Runx3*^{Tom} animals. No recombination was observed in *Phox2b*+ hindbrain visceromotor nuclei (DMV and NA), the locus coeruleus, or enteric ganglia (Figure S3A–S3E, S2I, and S2J; Table 1). In *Prox2*/*Runx3*^{Tom} animals, DRG neurons were not recombined, but 14.9% ± 1.5% of neurons of one single sympathetic ganglion, the celiac ganglion, and 14.1% ± 6.1% of geniculate neurons expressed tdTomato (Figures S2I, S2J, and S3F–S3I). In *Runx3*^{Tom} animals, few celiac (0.2% ± 0.3%), geniculate (4.1% ± 1.1%), and DRG (1.4% ± 0.1%) neurons were recombined (Figures S2I, S2J, and S3A–S3E). Recombination in other sympathetic ganglia was exceedingly rare in both *Prox2*/*Runx3*^{Tom} and *Runx3*^{Tom} animals (Figures S3F–S3H; see Table 1 for a summary).

In summary, *Prox2*/*Runx3*^{Tom} animals recombine both *Prox2*+ and *Runx3*+ vagal sensory neurons, and small subpopulations of celiac and geniculate neurons, whereas *Runx3*^{Tom} animals only recombine *Runx3*+ vagal neurons. Comparing the two strains can help to identify projections originating from their vagal difference, i.e., *Prox2*+ neurons.

Prox2/*Runx3* vagal neurons form IGLEs in the upper gastrointestinal tract

We investigated *Prox2* and *Runx3* vagal neuron innervation targets in the upper gastrointestinal tract using *Prox2*/*Runx3*^{Tom}

Figure 2. *Prox2*/*Runx3* neurons form IGLEs and IMAs in the upper gastrointestinal tract

(A) Light-sheet imaging (acquired by mesoscale selective plane illumination microscopy [mesoSPIM]) of the esophagus and stomach of *Prox2*/*Runx3*^{Tom} (left) and *Runx3*^{Tom} animals (right) showing tdTomato+ fibers (white). Scale bar, 2 mm.
(B) Immunohistology of esophageal IGLEs in *Prox2*/*Runx3*^{Tom} adult mice using antibodies against tdTomato. Scale bars, 200 μm (left) and 20 μm (right).
(C) Immunohistology of esophageal IGLEs in *Prox2*/*Runx3*^{Tom} (left) and *Runx3*^{Tom} animals (right) using tdTomato (red) and *Phox2b* (green) antibodies. Scale bar, 20 μm.
(D) Quantification of esophageal *Phox2b*+ enteric ganglia innervated by tdTomato+ fibers in *Prox2*/*Runx3*^{Tom} and *Runx3*^{Tom} animals on different axial levels; n = 3.
(E) Immunohistology of stomach IGLEs in *Prox2*/*Runx3*^{Tom} (left) and *Runx3*^{Tom} mice (right) using tdTomato (red) and *Phox2b* (green) antibodies. Scale bar, 20 μm.
(F) Quantification of *Phox2b*+ stomach enteric ganglia innervated by tdTomato+ fibers in *Prox2*/*Runx3*^{Tom} and *Runx3*^{Tom} animals in the glandular and non-glandular stomach, n = 3.
(G) Immunohistology of IMAs in *Prox2*/*Runx3*^{Tom} animals using tdTomato (red) and c-Kit (green) antibodies. Scale bar, 20 μm.
(H) Central synaptic connectivity of *Prox2*/*Runx3* neurons in the NTS. Scheme (top left) of the intersectional *FTLG* reporter allele labeling boutons with synaptophysinGFP in *Prox2*/*Runx3*^{SypGFP} (*Prox2*^{FlpO};*Phox2b*^{Cre};*R26*^{FTLG}) mice.⁴⁸ Immunohistology showing dense GFP+ boutons (green) in the NTS (middle left), on *Pou3f1*+ (red, bottom left) and TH+ (red, top right) NTS subtypes and on ChAT+ DMV neurons (red, bottom right). Scale bars, 200 μm. Data in (B) and (F) are represented as mean ± SD, **p < 0.01, ***p < 0.001, unpaired two-tailed t test. Images in (A), (D), (E), (G), and (H) were stitched using the tile-scan mode. See also Figures S2–S4.

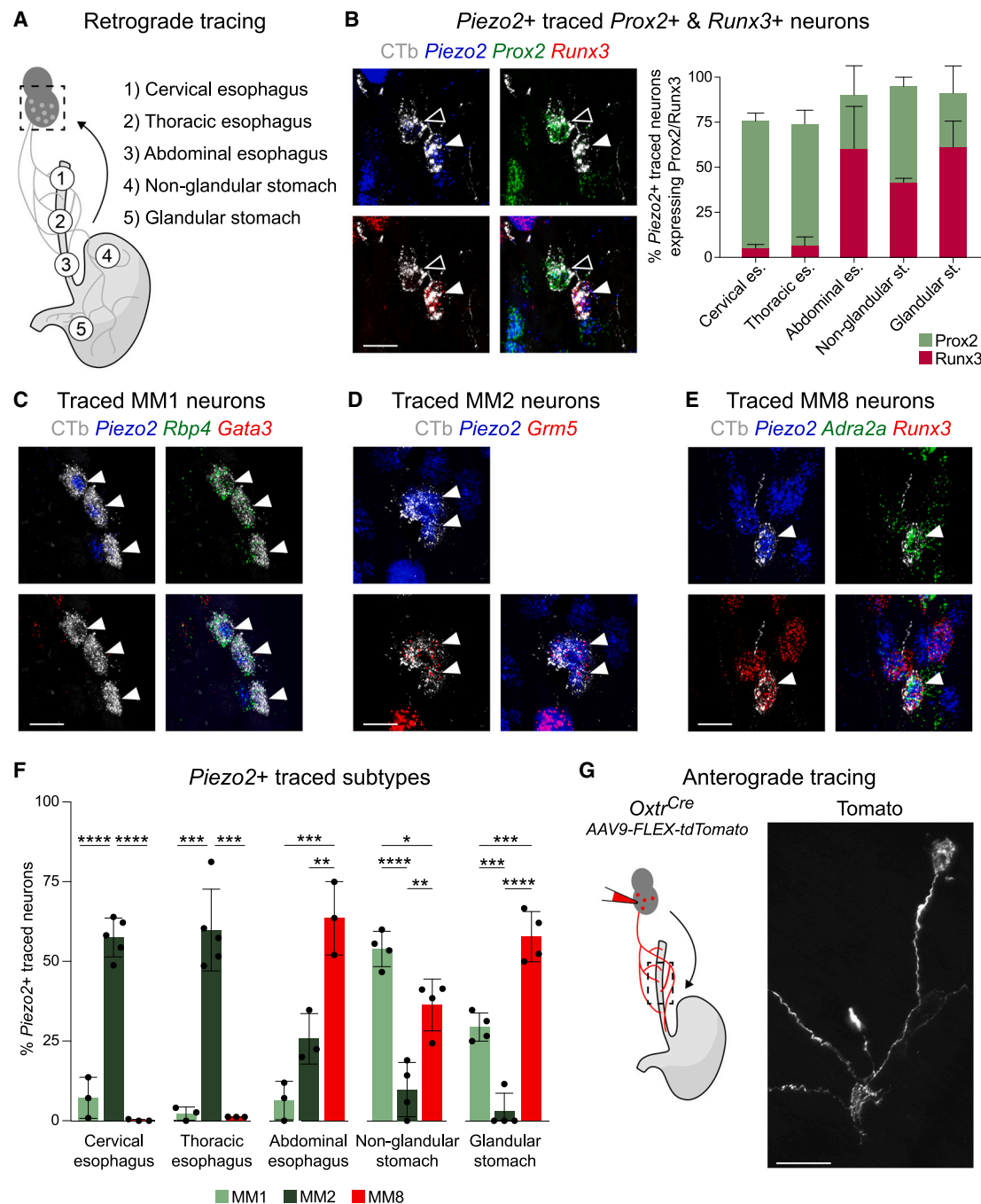


Figure 3. MM1, MM2, and MM8 subtypes of *Prox2*/*Runx3* vagal neurons innervate the upper digestive tract

(A) Scheme of retrograde tracing experiments.

(B) Left, smFISH analysis, combined with cholera toxin subunit b (CTb) (gray) immunohistology. Vagal neurons were analyzed after CTb injection into the abdominal esophagus; probes: *Prox2* (green), *Runx3* (red), and *Piezo2* (blue). A *Prox2*+*Piezo2*+CTb+ (open arrowhead) and *Runx3*+*Piezo2*+CTb+ (filled arrowhead) cell are indicated. Quantification of retrogradely labeled *Prox2*+*Piezo2*+ and *Runx3*+*Piezo2*+ neurons (right). We used Fast Blue to trace from the cervical and thoracic esophagus in postnatal P7 mice and CTb to trace from the abdominal esophagus and stomach in adult mice; n = 3–5. Scale bar, 20 μ m. (C–E) smFISH analysis of traced MM1, MM2, and MM8 neurons. CTb (gray) was detected by immunohistology. Probes used: (C) MM1: *Rbp4* (green), *Gata3* (red, negative marker), *Piezo2* (blue); (D) MM2: *Grm5* (green), *Piezo2* (blue); (E) MM8: *Adra2a* (green), *Runx3* (red), *Piezo2* (blue). Scale bars, 20 μ m.

(F) Quantification of traced MM1, MM2, and MM8 neurons (n = 3–5).

(G) (Left) Scheme of anterograde tracing in *Oxtr^{Cre}* mice by vagal injection of AAV9-FLEX-tdTomato. These anterograde tracing experiments revealed (right) esophageal IGLs (n = 6). Scale bar, 100 μ m. Data are represented as mean \pm SD, *p < 0.05, **p < 0.01, ***p < 0.001, ****p < 0.0001, ordinary one-way ANOVA with Tukey's multiple comparisons test. See also Figure S5.

Table 1. Recombination sites of Prox2/Runx3 neurons

| Location | Hindbrain nuclei/ganglia | Mouse line | Recombined neurons |
|-----------------------|-----------------------------------|----------------------------------|-------------------------|
| Hindbrain | locus coeruleus | <i>Prox2/Runx3^{Tom}</i> | 0%;0/1,983 neurons |
| | | <i>Runx3^{Tom}</i> | 0%;0/2,791 neurons |
| | nucleus ambiguus | <i>Prox2/Runx3^{Tom}</i> | 0%;0/592 neurons |
| | | <i>Runx3^{Tom}</i> | 0%;0/377 neurons |
| | dorsal motor nucleus of the vagus | <i>Prox2/Runx3^{Tom}</i> | 0%;0/2,114 neurons |
| | | <i>Runx3^{Tom}</i> | 0%;0/2,554 neurons |
| Upper digestive tract | esophagus enteric ganglia | <i>Prox2/Runx3^{Tom}</i> | 0%;0/419 neurons |
| | | <i>Runx3^{Tom}</i> | 0%;0/276 neurons |
| | stomach enteric ganglia | <i>Prox2/Runx3^{Tom}</i> | 0%;0/3,462 neurons |
| | | <i>Runx3^{Tom}</i> | 0%;0/3,199 neurons |
| Sympathetic ganglia | celiac ganglion | <i>Prox2/Runx3^{Tom}</i> | 15.0%;613/4,098 neurons |
| | | <i>Runx3^{Tom}</i> | 0.2%;8/4,132 neurons |
| | superior cervical ganglia | <i>Prox2/Runx3^{Tom}</i> | 0.02%;1/4,474 neurons |
| | | <i>Runx3^{Tom}</i> | 0.06%;4/6,534 neurons |
| | stellate ganglia | <i>Prox2/Runx3^{Tom}</i> | 0.13%;4/3,015 neurons |
| | | <i>Runx3^{Tom}</i> | 0.08%;5/6,567 neurons |
| | sympathetic chain ganglia | <i>Prox2/Runx3^{Tom}</i> | 0.12%;3/2,436 neurons |
| | | <i>Runx3^{Tom}</i> | 0.02%;1/4,341 neurons |
| Spinal afferents | dorsal root ganglia | <i>Prox2/Runx3^{Tom}</i> | 0%;0/17,049 neurons |
| | | <i>Runx3^{Tom}</i> | 1.4%;191/14,092 neurons |
| Other | geniculate ganglia | <i>Prox2/Runx3^{Tom}</i> | 15.0%;238/1,588 neurons |
| | | <i>Runx3^{Tom}</i> | 4.2%;56/1,342 neurons |

Neurons in the hindbrain, enteric ganglia in the upper digestive tract, sympathetic ganglia, geniculate ganglia, and DRGs were analyzed for recombination by assessment of tdTomato expression in both *Prox2/Runx3^{Tom}* and *Runx3^{Tom}* animals; see also Figure S3. Indicated are the locations/ganglia examined, mouse lines used, and total number of recombined neurons counted in 3 animals.

and *Runx3^{Tom}* mice (Figures 2A–2G). The esophagus and attached stomach were isolated, cleared, and imaged using light-sheet microscopy.^{49,50} The entire rostro-caudal axis of the esophagus was densely innervated by Prox2/Runx3 neurons but only sparsely by Runx3 vagal neurons (Figures 2A–2C). Quantifications demonstrated that the vast majority of esophageal ganglia in *Prox2/Runx3^{Tom}* mice, but few in *Runx3^{Tom}* mice, were contacted by tdTomato+ IGLs (Figure 2D). Thus, esophageal IGLs were mainly formed by Prox2 and, to a lesser extent, by Runx3 neurons.

In the stomach, we detected tdTomato+ IGLs in the glandular and non-glandular regions of *Prox2/Runx3^{Tom}* and *Runx3^{Tom}* animals (Figures 2A and 2E). *Runx3^{Tom}* animals showed a higher density of innervation in the glandular than the non-glandular stomach (Figures 2A and 2F). Thus, both Prox2 and Runx3 neurons form gastric IGLs, but preferentially innervate the non-glandular and glandular stomach, respectively. We did not detect tdTomato+ IGLs in the intestines of *Prox2/Runx3^{Tom}* animals, although we did find tdTomato+TH+ varicose endings on intestinal enteric ganglia that likely originate from the TH+ celiac ganglion (see below). tdTomato+ axons also made contacts with c-Kit+ interstitial cells of Cajal in the esophageal sphincter of *Prox2/Runx3^{Tom}*, but not *Runx3^{Tom}*, mice (Figure 2G). These endings correspond to IMAs. Rare tdTomato+ IMAs were detected in the stomachs of both *Prox2/Runx3^{Tom}* and *Runx3^{Tom}* mice.

Our scRNA-seq analysis indicated that Prox2/Runx3 vagal neurons encompass a large fraction of putative vagal mechanoreceptors, many of which were recently characterized by others. In accordance, we observed tdTomato+ endings in the lungs,⁵¹ laryngeal mucosa, and taste buds,¹² as well as in the aortic arch (Figures S4A–S4F).⁵² We additionally analyzed putative innervation sites of Prox2/Runx3 geniculate and celiac neurons. Prox2/Runx3 geniculate neurons formed tdTomato+ endings on the papillae of the tongue⁵³ (Figures S4G–S4I). Celiac *Prox2/Runx3^{Tom}* neurons co-express TH (Figure S2J) and are known to form varicose endings on intestinal ganglia and blood vessels.⁵⁴ tdTomato+TH+ nerve endings were absent in the esophagus and stomach but were observed in the intestine of *Prox2/Runx3^{Tom}* animals (Figures S4K–S4M). These tdTomato+ varicose endings contacted blood vessels and enteric neurons (Figures S4L and S4M); note that the morphology of varicose endings is distinct from IGLs (compare Figures 2C and S4M). In accordance with previous findings,⁵⁴ we suggest celiac neurons as a source of the intestinal tdTomato+ endings. Table 2 summarizes the organs innervated by Prox2/Runx3 vagal, geniculate, and celiac neurons.

Central projections of Prox2/Runx3 neurons

Vagal neurons project to second-order sensory neurons in the NTS. To define Prox2/Runx3 vagal neuron projections to the

Table 2. Innervation targets of Prox2/Runx3 neurons

| Ganglion | Target | Cell type | Subtype | Marker genes | Reference |
|---------------------|-------------------------|---|---------|---|--|
| Vagal | esophagus | enteric ganglia (IGLE) | MM2 | <i>Prox2+</i> , <i>Piezo2+</i> , <i>Grm5+</i> , <i>Glp1r</i> – | this work |
| | stomach (non-glandular) | enteric ganglia (IGLE) | MM1 | <i>Prox2+</i> , <i>Piezo2+</i> , <i>Glp1r+</i> , <i>Rbp4+</i> , <i>Gata3</i> – | this work; Williams et al. ¹³ |
| | stomach (glandular) | enteric ganglia (IGLE) | MM8 | <i>Runx3+</i> , <i>Prox2</i> ^{low} , <i>Piezo2+</i> , <i>Glp1r+</i> , <i>Adra2a+</i> | this work; Williams et al. ¹³ |
| | larynx | quadrangular membrane, mucosa, laryngeal taste buds | MM5 | <i>Runx3+</i> , <i>Slc18a3+</i> , <i>Pappa2+</i> , <i>P2ry1+</i> , <i>Piezo2</i> – | Prescott et al. ¹² |
| | lung | bronchi smooth muscle | MM10 | <i>Prox2+</i> , <i>Piezo2+</i> , <i>Lmcd1+</i> , <i>Sntg2+</i> , <i>Car2+</i> , <i>Slc17a7+</i> | Liu et al. ⁵¹ |
| | | neuroepithelial bodies | MM9 | <i>Runx3+</i> , <i>Piezo2+</i> , <i>Calb1+</i> , <i>Asic3+</i> , <i>Mafb+</i> | Liu et al. ⁵¹ |
| | heart | aortic arch | ? | <i>Mc4r+</i> , <i>Agtr1a+</i> | Min et al. ⁵² ; Zhao et al. ¹⁴ |
| Geniculate | tongue | taste buds | – | – | – |
| Celiac ^a | intestine | enteric ganglia (varicose endings); blood vessels | – | – | – |

Prox2/Runx3 neurons originating in the vagal, geniculate, and celiac ganglia innervate the indicated target organs and cell types/tissue; see also [Figures 2, 3, and S4](#). Listed are the names of vagal neuron subtype (for subtype nomenclature see [Figures 1D and 1E](#)) and the genes used here as markers to identify the subtypes. Previous work that characterized these vagal neuronal subtypes in depth are indicated in the references.

^aIn the intestine, we detected tdTomato+TH+ endings. Intestinal tdTomato+ varicose endings associated with enteric ganglia and blood vessels ([Figures S4K–S4M](#)). Varicose endings in the intestine were previously shown to be formed by celiac neurons.⁵⁴ The morphology of the endings thus suggests that these correspond to sympathetic efferents, but we cannot definitely exclude a vagal origin.

NTS, we labeled their synapses with synaptophysinGFP using *Prox2*^{FlpO};*Phox2b*^{Cre};*R26*^{FTLG} mice, hereafter named *Prox2/Runx3*^{SypGFP}.⁴⁸ This approach revealed many GFP+ synaptic boutons on Phox2b+ neurons in the NTS ([Figure 2H](#)). Using our unpublished scRNA-seq data of NTS neurons, we identified Pou3f1+ and thymidine hydroxylase+ (TH) interneurons in central and ventral nuclei of the NTS and observed that Prox2/Runx3 vagal sensory neurons formed synaptic boutons upon them. In accordance with previous reports,⁵⁵ we also found GFP+ boutons on choline acetyltransferase+ (ChAT) DMV neurons, but none on ChAT+ hypoglossal neurons ([Figure 2H](#)). Thus, Prox2/Runx3 vagal neurons project to Pou3f1+ and TH+ neurons in the NTS and directly to ChAT+ DMV neurons.

Prox2/Runx3 neurons innervate the upper gastrointestinal tract

Next, we defined the molecular subtype(s) of Prox2/Runx3 vagal neurons innervating the upper gastrointestinal tract by retrogradely labeling them from the cervical, thoracic, and abdominal esophagus, and from the glandular and non-glandular stomach (scheme in [Figure 3A](#)).^{56,57} smFISH was used to define *Prox2*, *Runx3*, and *Piezo2* expression in retrogradely traced vagal neurons. Overall, most traced *Piezo2*+ vagal neurons corresponded to Prox2 or Runx3 neuronal subtypes, i.e., ~75% from the cervical and thoracic esophagus and ~100% from the abdominal esophagus and stomach ([Figures 3B and S5A](#)). The upper esophagus is innervated by both superior (jugular) and inferior (nodose) vagal neurons,⁵⁸ and jugular neurons do not express Prox2. We suggest that jugular neurons represent the remaining

back-traced vagal *Prox2*-negative, *Piezo2*-positive cells in the cervical and thoracic esophagus.

Further analysis demonstrated that the Prox2 MM1 and MM2 as well as the Runx3 MM8 subtypes correspond to the *Piezo2*+ subtypes innervating the esophagus and stomach ([Figures 3C–3F](#)). These subtypes displayed preferences in their regional innervation. From the cervical and thoracic esophagus, mainly MM2 neurons were traced; MM2 neurons were less frequently traced from the abdominal esophagus, and rarely from the stomach ([Figure 3F](#)). The closely related MM1 subtype was often traced from the stomach ([Figure 3F](#)). MM8, a Runx3 subtype, was rarely traced from the cervical and thoracic esophagus, but frequently from the abdominal esophagus and stomach ([Figure 3F](#)). We detected further regional preferences in the glandular and non-glandular stomach ([Figure 3F](#)). Our assignment of vagal neurons innervating the stomach is supported by previous work that showed that *Glp1r*+ vagal neurons form gastric IGLEs,¹³ as *Glp1r* is expressed in the majority of MM1 (89.6% ± 5.3%) and MM8 (94.3% ± 2.6%), but not in MM2 neurons (2.4% ± 3.0%) ([Figures S5B and S5C](#)).

The majority of MM2, but not MM1 or MM8, neurons express *Oxtr* in the scRNA-seq data ([Figure S5D](#)). smFISH confirmed *Oxtr* expression in MM2 neurons, and demonstrated that almost all MM2+*Oxtr*+ neurons were recombined in *Prox2/Runx3*^{Tom} animals ([Figure S5E](#)). To verify that MM2 vagal neurons project to the esophagus, we directly injected the vagal ganglia of *Oxtr*^{Cre} mice with AAV9-FLEX-tdTomato. Analysis of the esophagus from injected animals demonstrated that the recombined vagal neurons identified by tdTomato expression formed esophageal

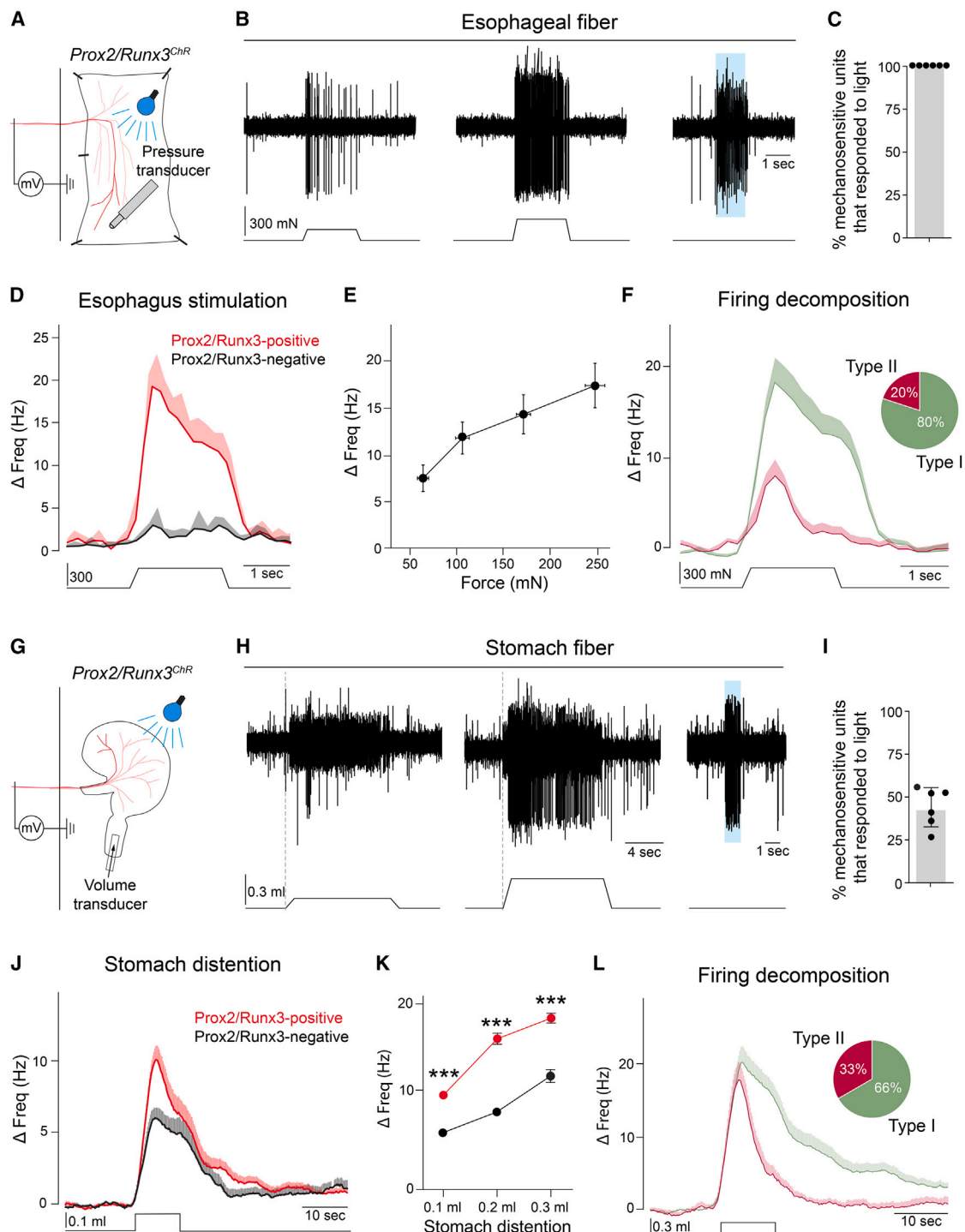


Figure 4. Prox2/Runx3 neurons are esophageal and gastric mechanoreceptors

(A) Scheme of the esophagus-vagus nerve *in vitro* preparation.

(B) Vagal fiber responding to mechanical stimuli of increasing strength (top); the intensity of the stimulus is indicated below (left, 100 mN; middle, 250 mN); note that the same fiber also responded to blue light in the absence of a mechanical stimulus (right).

(C) Quantification of Prox2/Runx3-positive units (30/30) among mechanosensitive units in the esophagus; n = 6 mice.

(D) Quantification of population firing patterns of Prox2/Runx3-positive (red) and -negative (black) units during mechanical stimulation (250 mN).

(E) Stimulus response properties of Prox2/Runx3-positive units to increasing mechanical force.

(F) Decomposition of Prox2/Runx3-positive unit firing patterns revealed two types of mechanosensory neurons (n = 30 units).

(legend continued on next page)

IGLEs (Figure 3G). We conclude that the MM1, MM2, and MM8 subtypes innervate the esophagus and stomach, where they end as IGLEs. The three subtypes display regional innervation preferences and, in particular, esophageal IGLEs are mainly formed by MM2 neurons.

Prox2/Runx3 vagal neurons are mechanoreceptors

We next investigated the electrophysiological properties of Prox2/Runx3 neurons using *Prox2/Runx3^{ChR}* (*Prox2^{FlpO};Phox2b^{Cre};Ai80*) mice to express channelrhodopsin in Prox2/Runx3 neurons.⁵⁹ The entire esophagus from these mice was isolated as an “open book” preparation, and the attached vagus nerve was used for recording responses in single nerve fibers (Figure 4A).^{8,60} Vagal fibers were classified as Prox2/Runx3-positive or -negative based on whether they fired action potentials in response to blue light (Figures 4B, S6A, and S6B). We applied mechanical stimuli using a piezo actuator, or shone blue light on the esophagus, and observed similar magnitude and firing kinetics in response to both stimuli in vagal fibers (Figure 4B). Interestingly, all mechanically sensitive vagal fibers identified in the thoracic and abdominal esophagus responded to blue light (30/30 neurons, Figures 4C and 4D). Thus, Prox2/Runx3-positive neurons are the sole vagal esophageal mechanoreceptors. Prox2/Runx3-positive neurons responded to forces ranging from 60 to 250 mN and increased their firing frequency in response to increasing force (Figure 4E). Analysis of single unit responses to mechanical stimuli revealed two distinct response patterns. The majority of the Prox2/Runx3-positive mechanoreceptors (80%) showed sustained firing of up to 20 Hz during stimulation, and firing frequency slowly returned to baseline after the end of the stimulation (we call these type I esophageal receptors; Figure 4F, green). The remaining 20% showed peak firing of around 7 Hz that returned to baseline before the end of the stimulus (type II esophageal receptors; Figure 4F, red). In summary, Prox2/Runx3-positive neurons form esophageal IGLEs and function as low-threshold mechanoreceptors. They segregate into type I and II receptors that differ in adaptation rates, and we suggest that these correspond to MM2 and MM8, respectively (see discussion).

In addition, we used an *in vitro* vagus-stomach preparation encompassing the entire stomach and the attached vagal trunk from *Prox2/Runx3^{ChR}* mice (Figure 4G). We administered physiological volumes of saline (0.1–0.3 mL) to distend the stomach.^{13,61} Around half of all neurons that responded to stomach distention were light-sensitive and thus corresponded to Prox2/Runx3-positive neurons (55/125 neurons; Figures 4H, 4I, and S6C). Across all volumes tested, light-sensitive fibers displayed higher firing rates in response to distention than light-insensitive fibers (Figures 4J and 4K). Closer examination of firing responses uncovered two distinct types (Figure 4L). Type I gastric receptors continued firing while the stomach was distended and only

returned to basal activity after the stomach had emptied, while type II gastric receptors reduced their firing frequency and quickly returned to basal activity—even while the stomach was still distended (Figure 4L). Thus, Prox2/Runx3-positive gastric vagal neurons are mechanosensitive and appear to detect static (type I) and dynamic changes in stretch (type II). We propose that type I and II gastric receptors correspond to MM1 and MM8, respectively (see discussion).

Ablation of Prox2/Runx3 neurons results in esophageal dysmotility

We used an intersectional genetic strategy to express the diphtheria toxin receptor (DTR) in Prox2/Runx3 neurons (*Prox2^{FlpO};Phox2b^{Cre};Tau^{ds-DTR}*, hereafter called *Prox2/Runx3^{ds-DTR}* mice).⁶² As the DTR receptor is only expressed after the removal of both lox- and frt-flanked stop cassettes, DT-treated *Prox2^{FlpO};Tau^{ds-DTR}* animals were used as controls (called *Control^{ds-DTR}*). DTR-expressing neurons were ablated by injecting diphtheria toxin (DT), and ablation efficacy and specificity were determined 2 weeks after DT injection by smFISH. This showed that the vast majority of Prox2+ and Runx3+ neurons were ablated in the vagal ganglia of *Prox2/Runx3^{ds-DTR}* animals (Figure 5A). Prox2/Runx3 neurons represent around 30% of all Phox2b+ vagal neurons and, in accordance, 32% ± 6% of Phox2b+ neurons were ablated after DT injection (Figure 5B). Following administration of DT, the animals' weight was monitored daily, which showed that *Prox2/Runx3^{ds-DTR}*, but not *Control^{ds-DTR}*, mice rapidly lost weight in the first 5 days post ablation (Figures 5C and S7A). *Prox2/Runx3^{ds-DTR}* animals received a high caloric diet and daily saline injections after ablation, which helped to stabilize their weight. VFSS allows the monitoring of swallowing behavior in freely moving animals (Figures 5D and 5E). We performed VFSS 2 days before and 19 days after ablation (see Figure S7B for an outline of the experiment, and Videos S1 and S2 for an example of the swallowing behavior before and after ablation).²⁸ The esophageal transit time of a liquid bolus increased from an average of 1.5 ± 0.4 to 39.3 ± 15.4 s after ablation (Figure 5F). Additionally, the liquid bolus was frequently retained in the esophagus, flowed in an oral direction to re-enter the pharynx (Video S3), and in some cases was regurgitated from the mouth. Such aberrant esophageal bolus movements were never observed before ablation. Swallowing difficulties were accompanied by megaesophagus, with the average diameter of their abdominal esophagus increasing from an average of 1.8 ± 0.2 mm before ablation to 2.8 ± 0.2 mm after ablation (Figure 5F). Moreover, numerous examples of aerophagia were observed after ablation (Video S4). Pharyngeal transit time and lick time were mildly increased, whereas the lick rate was slightly decreased (Figure 5F). Swallow rate, swallow interval, lick-to-swallow ratio, and jaw opening/closing

(G) Scheme of the stomach-vagus nerve *in vitro* preparation.

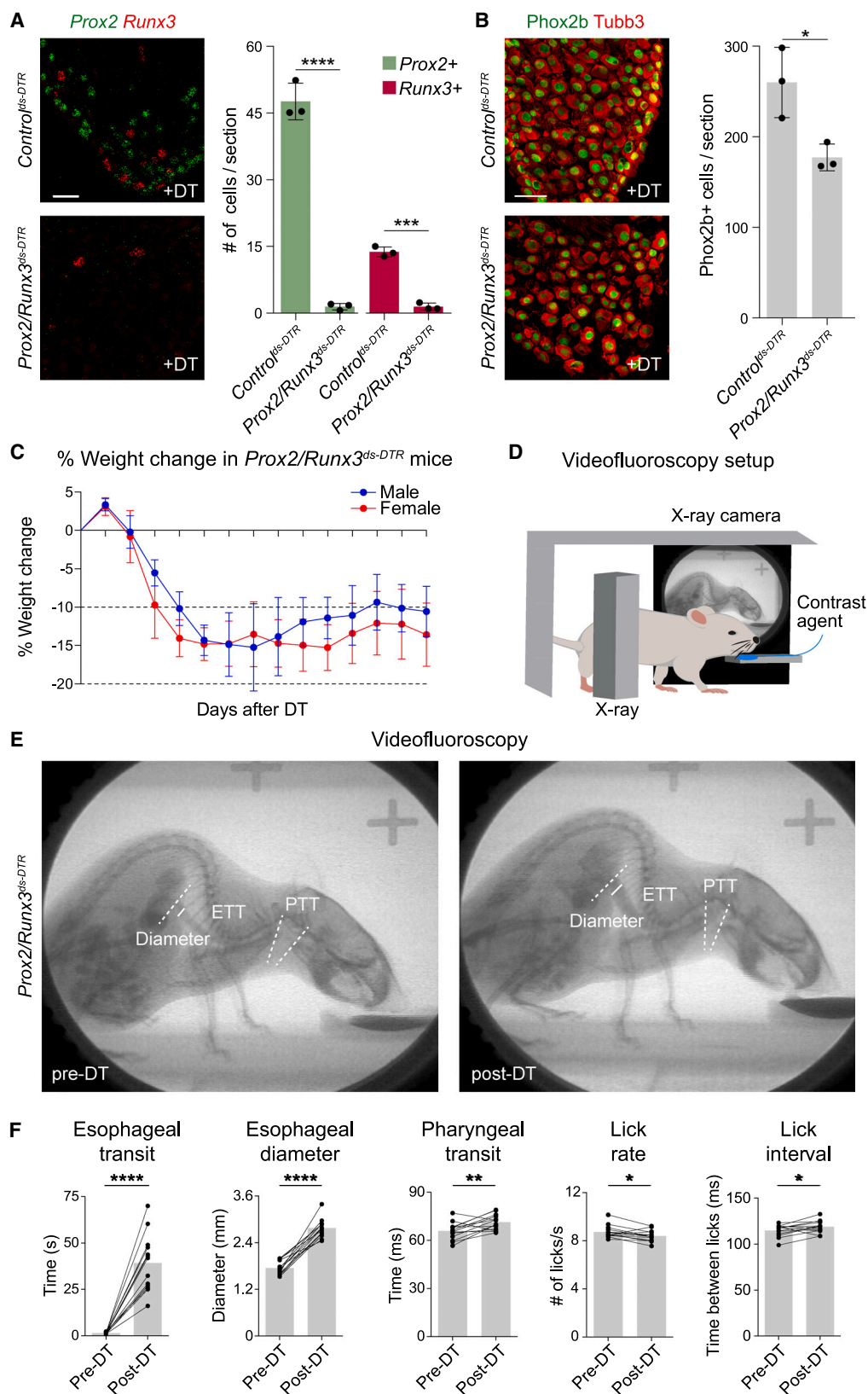
(H) Vagal fiber responding to the indicated distention and light stimuli.

(I) Proportions of Prox2/Runx3-positive units among all mechanosensitive units in the stomach (55/125 units, n = 6 mice).

(J) Population firing responses of Prox2/Runx3-positive (n = 54) and -negative (n = 36) units during stomach distention (0.1 mL).

(K) Stimulus response properties of Prox2/Runx3-positive (n = 45–54) and -negative (n = 35–43) units to increasing stomach distention (0.1–0.3 mL).

(L) Decomposition of Prox2/Runx3-positive unit firing patterns revealed two types (n = 46 units). Data are represented as mean ± SD (C and I) or mean ± SEM (D, E, F, J, K, and L), ***p < 0.001, unpaired two-tailed t test. See also Figure S6.



(legend on next page)

velocity were unaffected (Figure S7C). In summary, we observed severe deficits in ingestion after the ablation of Prox2/Runx3 neurons, which we assign to esophageal dysmotility.

DISCUSSION

Mechanosensory vagal neurons monitor esophageal and gastric distension. Here, we used genetically guided anatomical tracing and optogenetics to show that three vagal sensory neuronal subtypes that express *Prox2* and *Runx3* innervate the esophagus and stomach with regionalized specificity. All three subtypes form IGLs on enteric ganglia and function as low-threshold mechanoreceptors, but they display different adaptation properties (summarized in Figure 6). We used a genetic strategy to ablate Prox2/Runx3 neurons, and demonstrated that this resulted in dysphagia due to severe esophageal dysmotility in freely behaving animals. Our results reveal the importance of vagal sensory feedback provided by Prox2/Runx3 neurons in swallowing and food intake.

Prox2/Runx3 neurons innervate the esophagus and stomach

Prox2/Runx3 neurons represent the majority (~85%) of all *Piezo2*+ neurons in the nodose ganglion. They encompass eight neuronal subtypes, three of which (MM1, MM2, and MM8) form IGLs that innervate esophageal and gastric enteric ganglia. Comparisons of our molecular data with previously published analyses indicate the innervation targets of additional Prox2/Runx3 neurons. The MM9 and MM10 Prox2/Runx3 subtypes appear to correspond to neurons innervating the lung and MM5 to neurons innervating the larynx (summarized in Table 2).^{12,51} The assignment of the Prox2/Runx3 neuronal subtypes innervating the heart needs further investigation.

Together, the MM2 and MM8 subtypes of Prox2/Runx3 neurons innervate almost all (>95%) esophageal enteric ganglia, although most are innervated by MM2. Despite the morphological similarity of the nerve endings, we were able to distinguish between MM2 and MM8 neurons in genetically guided anatomical tracing experiments. The ablation of Prox2/Runx3 neurons demonstrated their importance in the esophageal phase of swallowing. Specifically, the ablation resulted in a dramatic increase in the transit time of a bolus through the esophagus, which was accompanied by megaeosophagus. Esophageal peristalsis is part of a complex motor sequence involving the consecutive and stereotypic contractions of pharyngeal and esophageal muscle groups. This intricate sequence of events is controlled by a central pattern generator

in the brainstem.⁶³ Deafferentation of the thoracic esophagus in sheep provided early evidence for a role of vagal sensory feedback in esophageal peristalsis.²⁵ Our data indicate that this feedback is essential for peristalsis and is provided by the MM2 and MM8 subtypes of Prox2/Runx3 neurons.

Despite the apparent morphological uniformity of IGLs, distinct vagal neuronal subtypes form these structures along the rostro-caudal axis of the gastrointestinal tract. Previous work showed that *Glp1r* marks neurons that form gastric IGLs.¹³ Here, we distinguish two *Glp1r*+ neuronal subtypes that innervate the stomach with regional preferences (MM1, MM8). Thus, gastric IGLs are more heterogeneous than previously recognized. Others described a subtype of vagal sensory neurons expressing *Oxtr* that forms IGLs on intestinal ganglia,¹⁰ but Prox2/Runx3 neurons do not form intestinal IGLs. The subtype identity of these intestinal *Oxtr*+ IGLs remains open. We show here that an additional subtype of esophageal IGLs is formed by MM2 neurons that also express *Oxtr*.

Electrophysiological properties of vagal Prox2/Runx3 neurons innervating the upper gastrointestinal tract

The optogenetic tools used here allowed us to assign the electrophysiological properties to specific subtypes of vagal Prox2/Runx3 neurons forming esophageal and gastric IGLs. Our retrograde tracing experiments demonstrated that Prox2/Runx3 neurons represent all vagal *Piezo2*+ neurons innervating the stomach. Nevertheless, Prox2/Runx3 neurons constituted only half of all mechanoreceptors detected by vagal fiber recordings that respond to stomach distention. Thus, *Piezo2*-negative vagal gastric mechanoreceptors exist, and they responded with lower firing frequencies to distention than *Piezo2*-positive mechanoreceptors. In the somatosensory system, genetic ablation of *Piezo2* leads to the loss or reduced mechanosensitivity of both rapidly and slowly adapting low-threshold mechanoreceptors.^{64–66} Work involving the genetic deletion of *Piezos* in vagal sensory neurons revealed their function in the control of breathing and blood pressure.^{67,68} Further studies are required to address the precise role of *Piezo2* in the Prox2/Runx3 vagal neurons innervating the gastrointestinal tract, to reveal the identity of the *Piezo2*-negative gastric vagal mechanoreceptors and to uncover the identity of the mechanosensitive channel(s) used by these neurons to detect stomach stretch.

In accordance with the molecular and anatomical data, our electrophysiological experiments uncovered different Prox2/Runx3 mechanoreceptive subtypes. Esophageal type I receptors adapted slower than type II receptors, and type I

Figure 5. Ablation of Prox2/Runx3 neurons impairs esophageal motility in freely behaving animals

(A) smFISH images (left) using *Prox2* (green) and *Runx3* (red) probes in adult *Control*^{ds-DTR} (top) and *Prox2/Runx3*^{ds-DTR} (bottom) mice 14 days after DT administration. (Right) Quantification; n = 3. Scale bar, 50 μ m.
(B) Immunofluorescence images (left) using Phox2b (green) and Tubb3 (red) antibodies in adult *Control*^{ds-DTR} (top) and *Prox2/Runx3*^{ds-DTR} (bottom) mice. (Right) Quantification; n = 3. Scale bar, 50 μ m.
(C) Weight change in *Prox2/Runx3*^{ds-DTR} mice after DT administration, n = 14.
(D) Scheme of the videofluoroscopy setup.
(E) X-ray images taken from the same *Prox2/Runx3*^{ds-DTR} mouse before (pre-DT, left) and after (post-DT, right) DT administration. Dotted lines show the bolus traveling distance used to determine pharyngeal transit time (PTT) and esophageal transit time (ETT). Solid line shows the site used to measure the esophageal diameter.
(F) Quantifications before and after ablation. Data are represented as mean \pm SD, *p < 0.05, **p < 0.01, ***p < 0.001, ****p < 0.0001, unpaired two-tailed t test (A and B), paired two-tailed t test (F). See also Figure S7.

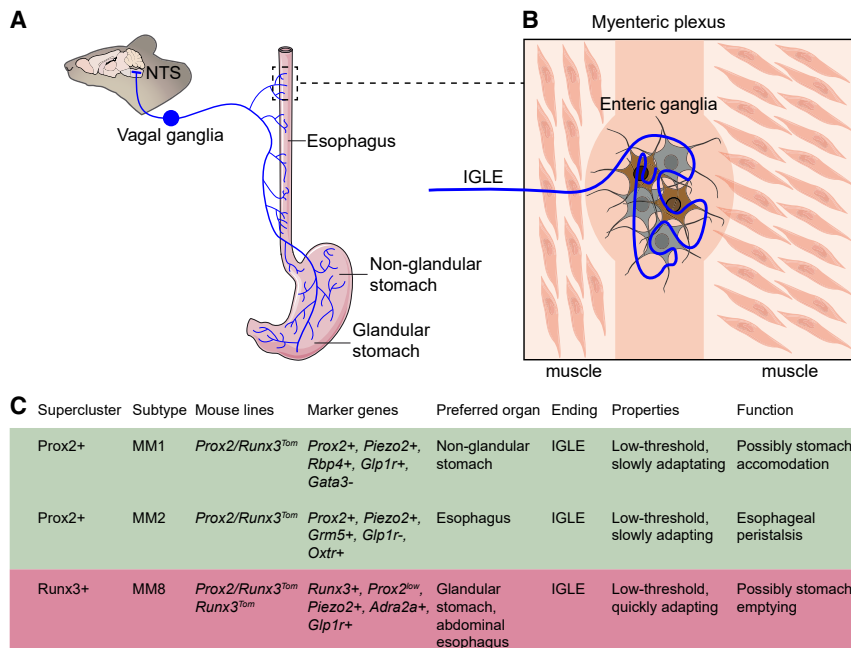


Figure 6. Summary

(A) Scheme of MM1, MM2, and MM8 vagal neurons and their targets. Illustrations were adapted from bioicons.com and scidraw.io and licensed under CC-BY 3.0 and CC-BY 4.0.

(B) Scheme of an MM2 IGLE contacting an esophageal enteric ganglion.

(C) Table summarizing the characteristics of MM1, MM2, and MM8 vagal neurons.

outnumbered type II mechanoreceptors four to one. MM2 is the most abundant *Prox2/Runx3* subtype innervating the esophagus. We therefore propose that MM2 corresponds to esophageal type I mechanoreceptors and MM8 to type II receptors. Esophageal distension mediates reflexes that result in contraction of the upper esophageal sphincter, and these differentially respond to slow and fast esophageal distension.^{26,69} Thus, MM2 and MM8 neurons might elicit different reflexes by encoding distinct aspects of esophageal distension.

Both gastric type I and esophageal type I receptors displayed similar adaptation properties. We propose that the gastric type I receptors correspond to MM1, which closely resembles the MM2 esophageal type I receptor in its molecular properties. Further, esophageal and gastric type II receptors display similar adaption properties, and we suggest that these correspond to the MM8 subtype. In accordance, a recent study recorded calcium activity in vagal neurons during stomach/esophagus distension and found that group C neurons, in particular *Piezo2+Glp1r+Rbp4+* and *Piezo2+Grm5+Slit2+* subtypes, display a slowly adapting response and appear to correspond to the *Prox2/Runx3* MM1 and MM2 subtypes, our proposed type I mechanoreceptors.¹⁴

The genetic ablation strategy used here affected vagal neuronal subtypes, among them the three subtypes (MM1, MM2, and MM8) that terminate as IGLEs in the esophagus and stomach, but not DRG neurons. Others recently showed that *Piezo2+* DRG neurons form intraganglionic varicose endings (IGVEs) in the stomach and that these regulate the speed of stomach emptying.⁷⁰ The VFSS setup used in this study allowed us to detect boli entering and leaving the stomach as well as stomach contractions, which were observable before and after ablation of *Prox2/Runx3* neurons. However, it lacked sufficient resolution to accurately quantify gastric contractions and emptying. The current gold standard for diagnosing gastric

paresis in patients is gastric emptying scintigraphy,^{71–73} which can also be used to study gastric motility in mice.⁷⁴

This technology could be employed in the future to define the relative contributions of vagal and DRG mechanoreceptors to various aspects of gastric physiology.

Neuronal control of esophageal motility

Abnormal esophageal motility encompasses a heterogeneous class of disorders, and hereditary, autoimmune, and infectious factors, as well as nervous system degeneration, were suggested to cause or contribute to the pathology.^{75,76} In humans, VFSS is used to diagnose and monitor swallowing dysfunction⁷⁷ and was recently adapted for use in rodents.^{28,78,79} We used VFSS to show that the ablation of *Prox2/Runx3* neurons results in marked esophageal dysmotility. The histological, retrograde, and anterograde tracing studies assign this function to the *Prox2/Runx3* neuronal subtypes that form IGLEs in the esophagus. The scRNA-seq datasets provide information on genes expressed in these neurons and can be mined for the identification of potential drug targets. This might be useful in modulating the vagal sensory neurons that control esophageal peristalsis, with the goal of ameliorating motility disorders.

In addition to the vagal sensory arm that provides the feedback needed for esophageal peristalsis, the sensorimotor circuit controlling esophageal motility includes the hindbrain central pattern generator in the NTS, as well as visceromotor effector neurons located in hindbrain motor nuclei—in particular the NA.^{4,15,17,63,80} The intersectional genetic approach relying on *Prox2^{FipO};Phox2b^{Cre}* affected the sensory arm but not the NTS or hindbrain motor nuclei. Our approach allowed us to perform experiments in freely behaving mice and avoided the caveats associated with viral technologies, such as variable and low recombination frequency or a risk of injury to muscles covering vagal ganglia. However, it also targeted neuronal subpopulations in the geniculate and celiac ganglia, as well as other types of vagal mechanoreceptors (summarized in [Tables 1 and 2](#)). Thus, ablated neuronal types other than vagal *Prox2/Runx3* innervating the esophagus may have contributed to the observed phenotypes. For instance, ablation of *Prox2/Runx3* neurons mildly affected swallowing parameters like pharyngeal transit time (~8% increase) and lick rate (~4% decrease),

whereas it had extremely pronounced effects on the esophageal phase of swallowing (~26-fold increase in transit time). Whether the mild changes in the pharyngeal transit time and lick rate are caused by the loss of targeted neuron types innervating the larynx or tongue, or indirectly by esophageal immobility, remains open.

STAR★METHODS

Detailed methods are provided in the online version of this paper and include the following:

- **KEY RESOURCES TABLE**
- **RESOURCE AVAILABILITY**
 - Lead contact
 - Materials availability
 - Data and code availability
- **EXPERIMENTAL MODEL AND SUBJECT DETAILS**
 - Mouse lines
- **METHOD DETAILS**
 - Vagal neuron isolation
 - Library generation and sequencing
 - Analysis of the P4 vagal ganglia CEL-Seq2 data
 - Integration analysis
 - Tissue preparation
 - Single molecule fluorescent *in situ* hybridization (RNA-scope) and immunohistology
 - Whole organ immunohistology and clearing
 - Retrograde tracing
 - Anterograde tracing
 - Generation of *Prox2^{FlpO}* mice
 - Esophagus and stomach single fiber nerve recordings and analysis
 - Ablation
 - Behavior
- **QUANTIFICATION AND STATISTICAL ANALYSIS**

SUPPLEMENTAL INFORMATION

Supplemental information can be found online at <https://doi.org/10.1016/j.neuron.2023.04.025>.

ACKNOWLEDGMENTS

We thank the following persons at the MDC Berlin: Bettina Brandt and Sven Buchert for technical assistance, Petra Stallerow and Claudia Päseler for animal husbandry, Thomas Müller for help with the submission and for critical reading of the manuscript, Fritz Rathjen for critically reading the manuscript, Hans-Peter Rahn (Flow Cytometry facility), Sandra Raimundo (Advanced Light Microscopy facility), and the staff of the Next Generation Sequencing facility for their help. In addition, we thank the University of Missouri veterinary staff and pathology laboratory for the monitoring of mice and the authors of Bai et al.¹⁰ for providing scRNA-seq data. We also thank Mohammed Khallaf and Julia Ojeda-Alonso for help in establishing the *ex vivo* esophagus/stomach vagal nerve preparation. E.D.L. was supported by a Travelling Fellowship from the Company of Biologists (grant no. DEVTF2103518) and an MDC Internal PhD Fellowship. This work was supported by the Deutsche Forschungsgemeinschaft (DFG) under Germany's Excellence Strategy (EXC-2049 – 39068808) and by the Helmholtz Association (to C.B.).

AUTHOR CONTRIBUTIONS

Conceptualization, E.D.L. and C.B.; methodology, E.D.L., P.-L.R., A.M., K.S., N.V., K.L.O., X.L., G.R.L., T.E.L., and R.S.G.; software, A.M.; validation, R.T. and T.E.L.; formal analysis, E.D.L., P.-L.R., A.M., and S.D.; investigation, E.D.L., P.-L.R., A.M., K.L.O., T.E.L., H.L., and R.S.G.; resources, C.B., J.-F.B., A.W., N.Z., R.K., S.J., G.R.L., N.R., and T.E.L.; data curation, A.M.; writing, E.D.L. and C.B.; supervision, C.B., S.J., N.R., T.E.L., and S.D.L.

DECLARATION OF INTERESTS

S.D.L. is a consultant for Kallyope.

INCLUSION AND DIVERSITY

We support inclusive, diverse, and equitable conduct of research.

Received: June 28, 2022

Revised: October 31, 2022

Accepted: April 24, 2023

Published: May 15, 2023

REFERENCES

1. Prescott, S.L., and Liberles, S.D. (2022). Internal senses of the vagus nerve. *Neuron* 110, 579–599. <https://doi.org/10.1016/j.neuron.2021.12.020>.
2. Brookes, S.J., Spencer, N.J., Costa, M., and Zagorodnyuk, V.P. (2013). Extrinsic primary afferent signalling in the gut. *Nat. Rev. Gastroenterol. Hepatol.* 10, 286–296. <https://doi.org/10.1038/nrgastro.2013.29>.
3. Mercado-Perez, A., and Beyder, A. (2022). Gut feelings: mechanosensing in the gastrointestinal tract. *Nat. Rev. Gastroenterol. Hepatol.* 19, 283–296. <https://doi.org/10.1038/s41575-021-00561-y>.
4. Kim, M., Heo, G., and Kim, S.Y. (2022). Neural signalling of gut mechanosensation in ingestive and digestive processes. *Nat. Rev. Neurosci.* 23, 135–156. <https://doi.org/10.1038/s41583-021-00544-7>.
5. Phillips, R.J., and Powley, T.L. (2000). Tension and stretch receptors in gastrointestinal smooth muscle: re-evaluating vagal mechanoreceptor electrophysiology. *Brain Res. Brain Res. Rev.* 34, 1–26. [https://doi.org/10.1016/S0165-0173\(00\)00036-9](https://doi.org/10.1016/S0165-0173(00)00036-9).
6. Wang, F.B., and Powley, T.L. (2000). Topographic inventories of vagal afferents in gastrointestinal muscle. *J. Comp. Neurol.* 421, 302–324. [https://doi.org/10.1002/\(SICI\)1096-9861\(20000605\)421:3<302::AID-CNE2>3.0.CO;2-N](https://doi.org/10.1002/(SICI)1096-9861(20000605)421:3<302::AID-CNE2>3.0.CO;2-N).
7. Zagorodnyuk, V.P., and Brookes, S.J. (2000). Transduction sites of vagal mechanoreceptors in the guinea pig esophagus. *J. Neurosci.* 20, 6249–6255. <https://doi.org/10.1523/JNEUROSCI.20-16-06249.2000>.
8. Page, A.J., Martin, C.M., and Blackshaw, L.A. (2002). Vagal mechanoreceptors and chemoreceptors in mouse stomach and esophagus. *J. Neurophysiol.* 87, 2095–2103. <https://doi.org/10.1152/jn.00785.2001>.
9. Zagorodnyuk, V.P., Chen, B.N., Costa, M., and Brookes, S.J. (2003). Mechanotransduction by intraganglionic laminar endings of vagal tension receptors in the guinea-pig oesophagus. *J. Physiol.* 553, 575–587. <https://doi.org/10.1113/jphysiol.2003.051862>.
10. Bai, L., Mesgarzadeh, S., Ramesh, K.S., Huey, E.L., Liu, Y., Gray, L.A., Aitken, T.J., Chen, Y., Beutler, L.R., Ahn, J.S., et al. (2019). Genetic identification of vagal sensory neurons that control feeding. *Cell* 179, 1129.e23–1143.e23. <https://doi.org/10.1016/j.cell.2019.10.031>.
11. Kupari, J., Häring, M., Agirre, E., Castelo-Branco, G., and Ernfors, P. (2019). An atlas of vagal sensory neurons and their molecular specialization. *Cell Rep.* 27, 2508.e4–2523.e4. <https://doi.org/10.1016/j.celrep.2019.04.096>.
12. Prescott, S.L., Umans, B.D., Williams, E.K., Brust, R.D., and Liberles, S.D. (2020). An airway protection program revealed by sweeping genetic

- control of vagal afferents. *Cell* 181, 574.e14–589.e14. <https://doi.org/10.1016/j.cell.2020.03.004>.
13. Williams, E.K., Chang, R.B., Strohlic, D.E., Umans, B.D., Lowell, B.B., and Liberles, S.D. (2016). Sensory neurons that detect stretch and nutrients in the digestive system. *Cell* 166, 209–221. <https://doi.org/10.1016/j.cell.2016.05.011>.
14. Zhao, Q., Yu, C.D., Wang, R., Xu, Q.J., Dai Pra, R., Zhang, L., and Chang, R.B. (2022). A multidimensional coding architecture of the vagal interoceptive system. *Nature* 603, 878–884. <https://doi.org/10.1038/s41586-022-04515-5>.
15. Goyal, R.K., and Chaudhury, A. (2008). Physiology of normal esophageal motility. *J. Clin. Gastroenterol.* 42, 610–619. <https://doi.org/10.1097/MCG.0b013e31816b444d>.
16. Ertekin, C., and Aydogdu, I. (2003). Neurophysiology of swallowing. *Clin. Neurophysiol.* 114, 2226–2244. [https://doi.org/10.1016/s1388-2457\(03\)00237-2](https://doi.org/10.1016/s1388-2457(03)00237-2).
17. Coverdell, T.C., Abraham-Fan, R.J., Wu, C., Abbott, S.B.G., and Campbell, J.N. (2022). Genetic encoding of an esophageal motor circuit. *Cell Rep.* 39, 110962. <https://doi.org/10.1016/j.celrep.2022.110962>.
18. Aslam, M., and Vaezi, M.F. (2013). Dysphagia in the elderly. *Gastroenterol. Hepatol. (N Y)* 9, 784–795.
19. Suttrup, I., and Warnecke, T. (2016). Dysphagia in Parkinson's disease. *Dysphagia* 31, 24–32. <https://doi.org/10.1007/s00455-015-9671-9>.
20. Aziz, Q., Fass, R., Gyawali, C.P., Miwa, H., Pandolfino, J.E., and Zerbib, F. (2016). Functional esophageal disorders. *Gastroenterology* 150, 1368–1379. <https://doi.org/10.1053/j.gastro.2016.02.012>.
21. Kloepper, A., Arnold, J., Ruffolo, A., Kinealy, B., Haxton, C., Nichols, N., Takahashi, K., and Lever, T.E. (2020). An experimental swallow evoked potential protocol to investigate the neural substrates of swallowing. *OTO Open* 4, 2473974X20913542. <https://doi.org/10.1177/2473974X20913542>.
22. Kronecker, H., and Melzer, S. (1883). *Der Schluckmechanismus, seine Erregung und seine Hemmung*. *Arch Anat Physiol. Physiol. Abt. Suppl.* 328–360.
23. Janssens, J., De Wever, I., Vantrappen, G., and Hellemans, J. (1976). Peristalsis in smooth muscle esophagus after transection and bolus deviation. *Gastroenterology* 71, 1004–1009. [https://doi.org/10.1016/S0016-5085\(76\)80049-2](https://doi.org/10.1016/S0016-5085(76)80049-2).
24. Jean, A. (1984). Brainstem organization of the swallowing network. *Brain Behav. Evol.* 25, 109–116. <https://doi.org/10.1159/000118856>.
25. Falempin, M., Madhloum, A., and Rousseau, J.P. (1986). Effects of vagal deafferentation on oesophageal motility and transit in the sheep. *J. Physiol.* 372, 425–436. <https://doi.org/10.1113/jphysiol.1986.sp016017>.
26. Lang, I.M. (2009). Brain stem control of the phases of swallowing. *Dysphagia* 24, 333–348. <https://doi.org/10.1007/s00455-009-9211-6>.
27. Frazure, M.L., Brown, A.D., Greene, C.L., Iceman, K.E., and Pitts, T. (2021). Rapid activation of esophageal mechanoreceptors alters the pharyngeal phase of swallow: evidence for inspiratory activity during swallow. *PLoS One* 16, e0248994. <https://doi.org/10.1371/journal.pone.0248994>.
28. Lever, T.E., Braun, S.M., Brooks, R.T., Harris, R.A., Littrell, L.L., Neff, R.M., Hinkel, C.J., Allen, M.J., and Ulsas, M.A. (2015). Adapting human video-fluoroscopic swallow study methods to detect and characterize dysphagia in murine disease models. *J. Vis. Exp.* 52319. <https://doi.org/10.3791/52319>.
29. Hinkel, C.J., Sharma, R., Thakkar, M.M., Takahashi, K., Hopewell, B.L., and Lever, T.E. (2016). Neural mechanisms contributing to dysphagia in mouse models. *Otolaryngol. Head Neck Surg.* 155, 303–306. <https://doi.org/10.1177/0194599816640261>.
30. Haney, M.M., Sinnott, J., Osman, K.L., Deninger, I., Andel, E., Caywood, V., Mok, A., Ballenger, B., Cummings, K., Thombs, L., et al. (2019). Mice lacking brain-derived serotonin have altered swallowing function. *Otolaryngol. Head Neck Surg.* 161, 468–471. <https://doi.org/10.1177/0194599819846109>.
31. Hashimshony, T., Senderovich, N., Avital, G., Klochendler, A., de Leeuw, Y., Anavy, L., Gennert, D., Li, S., Livak, K.J., Rozenblatt-Rosen, O., et al. (2016). CEL-Seq2: sensitive highly-multiplexed single-cell RNA-Seq. *Genome Biol.* 17, 77. <https://doi.org/10.1186/s13059-016-0938-8>.
32. Kim, M., Franke, V., Brandt, B., Lowenstein, E.D., Schöwel, V., Spuler, S., Akalin, A., and Birchmeier, C. (2020). Single-nucleus transcriptomics reveals functional compartmentalization in syncytial skeletal muscle cells. *Nat. Commun.* 11, 6375. <https://doi.org/10.1038/s41467-020-20064-9>.
33. Ayer-Le Lievre, C.S., and Le Douarin, N.M. (1982). The early development of cranial sensory ganglia and the potentialities of their component cells studied in quail-chick chimeras. *Dev. Biol.* 94, 291–310. [https://doi.org/10.1016/0012-1606\(82\)90349-9](https://doi.org/10.1016/0012-1606(82)90349-9).
34. D'Amico-Martel, A., and Noden, D.M. (1983). Contributions of placodal and neural crest cells to avian cranial peripheral ganglia. *Am. J. Anat.* 166, 445–468. <https://doi.org/10.1002/aja.1001660406>.
35. Pattyn, A., Morin, X., Cremer, H., Goridis, C., and Brunet, J.F. (1999). The homeobox gene *Phox2b* is essential for the development of autonomic neural crest derivatives. *Nature* 399, 366–370. <https://doi.org/10.1038/20700>.
36. D'Autréaux, F., Coppola, E., Hirsch, M.R., Birchmeier, C., and Brunet, J.F. (2011). Homeoprotein *Phox2b* commands a somatic-to-visceral switch in cranial sensory pathways. *Proc. Natl. Acad. Sci. USA* 108, 20018–20023. <https://doi.org/10.1073/pnas.1110416108>.
37. Coste, B., Mathur, J., Schmidt, M., Earley, T.J., Ranade, S., Petrus, M.J., Dubin, A.E., and Patapoutian, A. (2010). *Piezo1* and *Piezo2* are essential components of distinct mechanically activated cation channels. *Science* 330, 55–60. <https://doi.org/10.1126/science.1193270>.
38. Murthy, S.E., Dubin, A.E., and Patapoutian, A. (2017). Piezos thrive under pressure: mechanically activated ion channels in health and disease. *Nat. Rev. Mol. Cell Biol.* 18, 771–783. <https://doi.org/10.1038/nrm.2017.92>.
39. Ranade, S.S., Syeda, R., and Patapoutian, A. (2015). Mechanically activated ion channels. *Neuron* 87, 1162–1179. <https://doi.org/10.1016/j.neuron.2015.08.032>.
40. Nishijima, I., and Ohtoshi, A. (2006). Characterization of a novel prospero-related homeobox gene, *Prox2*. *Mol. Genet. Genomics* 275, 471–478. <https://doi.org/10.1007/s00438-006-0105-0>.
41. Patthey, C., Clifford, H., Haerty, W., Ponting, C.P., Shimeld, S.M., and Begbie, J. (2016). Identification of molecular signatures specific for distinct cranial sensory ganglia in the developing chick. *Neural Dev.* 11, 3. <https://doi.org/10.1186/s13064-016-0057-y>.
42. Dvoryanchikov, G., Hernandez, D., Roebber, J.K., Hill, D.L., Roper, S.D., and Chaudhari, N. (2017). Transcriptomes and neurotransmitter profiles of classes of gustatory and somatosensory neurons in the geniculate ganglion. *Nat. Commun.* 8, 760. <https://doi.org/10.1038/s41467-017-01095-1>.
43. Anderson, C.B., and Larson, E.D. (2020). Single cell transcriptional profiling of *Phox2b*-expressing geniculate ganglion neurons. Preprint at bioRxiv. <https://doi.org/10.1101/812578>.
44. Allen Institute for Brain Science (2013). Developing Mouse Brain Atlas (Allen Institute for Brain Science). <http://www.brain-map.org>.
45. Levanon, D., Bernstein, Y., Negreanu, V., Bone, K.R., Pozner, A., Eilam, R., Lotem, J., Brenner, O., and Groner, Y. (2011). Absence of *Runx3* expression in normal gastrointestinal epithelium calls into question its tumour suppressor function. *EMBO Mol. Med.* 3, 593–604. <https://doi.org/10.1002/emmm.201100168>.
46. Levanon, D., Bettoun, D., Harris-Cerruti, C., Woolf, E., Negreanu, V., Eilam, R., Bernstein, Y., Goldenberg, D., Xiao, C., Fliegau, M., et al. (2002). The *Runx3* transcription factor regulates development and survival of *TrkC* dorsal root ganglia neurons. *EMBO J.* 21, 3454–3463. <https://doi.org/10.1093/emboj/cdf370>.
47. Shin, B., Hosokawa, H., Romero-Wolf, M., Zhou, W., Masuhara, K., Tobin, V.R., Levanon, D., Groner, Y., and Rothenberg, E.V. (2021). *Runx1* and *Runx3* drive progenitor to T-lineage transcriptome conversion in mouse

- T cell commitment via dynamic genomic site switching. *Proc. Natl. Acad. Sci. USA* 118. <https://doi.org/10.1073/pnas.2019655118>.
48. Dempsey, B., Sungelee, S., Bokiniec, P., Chettouh, Z., Diem, S., Autran, S., Harrell, E.R., Poulet, J.F.A., Birchmeier, C., Carey, H., et al. (2021). A medullary centre for lapping in mice. *Nat. Commun.* 12, 6307. <https://doi.org/10.1038/s41467-021-26275-y>.
 49. Susaki, E.A., Tainaka, K., Perrin, D., Yukinaga, H., Kuno, A., and Ueda, H.R. (2015). Advanced CUBIC protocols for whole-brain and whole-body clearing and imaging. *Nat. Protoc.* 10, 1709–1727. <https://doi.org/10.1038/nprot.2015.085>.
 50. Voigt, F.F., Kirschenbaum, D., Platonova, E., Pagès, S., Campbell, R.A.A., Kastli, R., Schaettin, M., Egolf, L., van der Bourg, A., Bethge, P., et al. (2019). The mesoSPIM initiative: open-source light-sheet microscopes for imaging cleared tissue. *Nat. Methods* 16, 1105–1108. <https://doi.org/10.1038/s41592-019-0554-0>.
 51. Liu, Y., Diaz de Arce, A.J., and Krasnow, M.A. (2021). Molecular, anatomical, and functional organization of lung interoceptors. Preprint at bioRxiv. <https://doi.org/10.1101/2021.11.10.468116>.
 52. Min, S., Chang, R.B., Prescott, S.L., Beeler, B., Joshi, N.R., Strohlic, D.E., and Liberles, S.D. (2019). Arterial baroreceptors sense blood pressure through decorated aortic claws. *Cell Rep.* 29, 2192.e3–2201.e3. <https://doi.org/10.1016/j.celrep.2019.10.040>.
 53. Frank, M.E. (1991). Taste-responsive neurons of the glossopharyngeal nerve of the rat. *J. Neurophysiol.* 65, 1452–1463. <https://doi.org/10.1152/jn.1991.65.6.1452>.
 54. Walter, G.C., Phillips, R.J., McAdams, J.L., and Powley, T.L. (2016). Individual sympathetic postganglionic neurons coinnervate myenteric ganglia and smooth muscle layers in the gastrointestinal tract of the rat. *J. Comp. Neurol.* 524, 2577–2603. <https://doi.org/10.1002/cne.23978>.
 55. Bassi, J.K., Connelly, A.A., Butler, A.G., Liu, Y., Ghanbari, A., Farmer, D.G.S., Jenkins, M.W., Melo, M.R., McDougall, S.J., and Allen, A.M. (2022). Analysis of the distribution of vagal afferent projections from different peripheral organs to the nucleus of the solitary tract in rats. *J. Comp. Neurol.* 530, 3072–3103. <https://doi.org/10.1002/cne.25398>.
 56. Stoeckel, K., Schwab, M., and Thoenen, H. (1977). Role of gangliosides in the uptake and retrograde axonal transport of cholera and tetanus toxin as compared to nerve growth factor and wheat germ agglutinin. *Brain Res.* 132, 273–285. [https://doi.org/10.1016/0006-8993\(77\)90421-8](https://doi.org/10.1016/0006-8993(77)90421-8).
 57. Bentivoglio, M., Kuypers, H.G., Catsman-Berrevorts, C.E., Loewe, H., and Dann, O. (1980). Two new fluorescent retrograde neuronal tracers which are transported over long distances. *Neurosci. Lett.* 18, 25–30. [https://doi.org/10.1016/0304-3940\(80\)90208-6](https://doi.org/10.1016/0304-3940(80)90208-6).
 58. Kwong, K., Kollarik, M., Nassenstein, C., Ru, F., and Undem, B.J. (2008). P2X2 receptors differentiate placodal vs. neural crest C-fiber phenotypes innervating guinea pig lungs and esophagus. *Am. J. Physiol. Lung Cell. Mol. Physiol.* 295, L858–L865. <https://doi.org/10.1152/ajplung.90360.2008>.
 59. Daigle, T.L., Madisen, L., Hage, T.A., Valley, M.T., Knoblich, U., Larsen, R.S., Takeno, M.M., Huang, L., Gu, H., Larsen, R., et al. (2018). A suite of transgenic driver and reporter mouse lines with enhanced brain-cell-type targeting and functionality. *Cell* 174, 465.e22–480.e22. <https://doi.org/10.1016/j.cell.2018.06.035>.
 60. Page, A.J., and Blackshaw, L.A. (1998). An in vitro study of the properties of vagal afferent fibres innervating the ferret oesophagus and stomach. *J. Physiol.* 512, 907–916. <https://doi.org/10.1111/j.1469-7793.1998.907bd.x>.
 61. Kim, D.Y., Heo, G., Kim, M., Kim, H., Jin, J.A., Kim, H.K., Jung, S., An, M., Ahn, B.H., Park, J.H., et al. (2020). A neural circuit mechanism for mechanosensory feedback control of ingestion. *Nature* 580, 376–380. <https://doi.org/10.1038/s41586-020-2167-2>.
 62. Britz, O., Zhang, J., Grossmann, K.S., Dyck, J., Kim, J.C., Dymecki, S., Gosgnach, S., and Goulding, M. (2015). A genetically defined asymmetry underlies the inhibitory control of flexor-extensor locomotor movements. *eLife* 4. <https://doi.org/10.7554/eLife.04718>.
 63. Jean, A. (2001). Brain stem control of swallowing: neuronal network and cellular mechanisms. *Physiol. Rev.* 81, 929–969. <https://doi.org/10.1152/physrev.2001.81.2.929>.
 64. Ranade, S.S., Woo, S.H., Dubin, A.E., Moshourab, R.A., Wetzel, C., Petrus, M., Mathur, J., Bégay, V., Coste, B., Mainquist, J., et al. (2014). Piezo2 is the major transducer of mechanical forces for touch sensation in mice. *Nature* 516, 121–125. <https://doi.org/10.1038/nature13980>.
 65. Woo, S.H., Ranade, S., Weyer, A.D., Dubin, A.E., Baba, Y., Qiu, Z., Petrus, M., Miyamoto, T., Reddy, K., Lumpkin, E.A., et al. (2014). Piezo2 is required for Merkel-cell mechanotransduction. *Nature* 509, 622–626. <https://doi.org/10.1038/nature13251>.
 66. Murthy, S.E., Loud, M.C., Daou, I., Marshall, K.L., Schwaller, F., Kühnemund, J., Francisco, A.G., Keenan, W.T., Dubin, A.E., Lewin, G.R., et al. (2018). The mechanosensitive ion channel Piezo2 mediates sensitivity to mechanical pain in mice. *Sci. Transl. Med.* 10. <https://doi.org/10.1126/scitranslmed.aat9897>.
 67. Nonomura, K., Woo, S.H., Chang, R.B., Gillich, A., Qiu, Z., Francisco, A.G., Ranade, S.S., Liberles, S.D., and Patapoutian, A. (2017). Piezo2 senses airway stretch and mediates lung inflation-induced apnoea. *Nature* 541, 176–181. <https://doi.org/10.1038/nature20793>.
 68. Zeng, W.Z., Marshall, K.L., Min, S., Daou, I., Chapeau, M.W., Abboud, F.M., Liberles, S.D., and Patapoutian, A. (2018). PIEZO2 mediates neuronal sensing of blood pressure and the baroreceptor reflex. *Science* 362, 464–467. <https://doi.org/10.1126/science.aau6324>.
 69. Lang, I.M., Medda, B.K., and Shaker, R. (2001). Mechanisms of reflexes induced by esophageal distension. *Am. J. Physiol. Gastrointest. Liver Physiol.* 281, G1246–G1263. <https://doi.org/10.1152/ajpgi.2001.281.5.G1246>.
 70. Servin-Vences, M.R., Lam, R.M., Koolen, A., Wang, Y., Saade, D.N., Loud, M., Kacmaz, H., Beyder, A., Marshall, K.L., Bönnemann, C.G., et al. (2022). PIEZO2 in somatosensory neurons controls gastrointestinal transit. Preprint at bioRxiv. <https://doi.org/10.1101/2022.11.27.518109>.
 71. Hasler, W.L. (2011). Gastroparesis: pathogenesis, diagnosis and management. *Nat. Rev. Gastroenterol. Hepatol.* 8, 438–453. <https://doi.org/10.1038/nrgastro.2011.116>.
 72. Grover, M., Farrugia, G., and Stanghellini, V. (2019). Gastroparesis: a turning point in understanding and treatment. *Gut* 68, 2238–2250. <https://doi.org/10.1136/gutjnl-2019-318712>.
 73. Ora, M., Nazar, A.H., Parashar, A., Kheruka, S., and Gambhir, S. (2019). Gastric emptying scintigraphy: beyond numbers - an observational study to differentiate between various etiologies and a step toward personalized management. *Indian J. Nucl. Med.* 34, 194–200. https://doi.org/10.4103/ijnm.IJNM_55_19.
 74. Bennink, R.J., De Jonge, W.J., Symonds, E.L., van den Wijngaard, R.M., Spijkerboer, A.L., Benninga, M.A., and Boeckstaens, G.E. (2003). Validation of gastric-emptying scintigraphy of solids and liquids in mice using dedicated animal pinhole scintigraphy. *J. Nucl. Med.* 44, 1099–1104.
 75. Kahrilas, P.J., Bredenoord, A.J., Fox, M., Gyawali, C.P., Roman, S., Smout, A.J., and Pandolfino, J.E.; International High Resolution Manometry Working Group (2015). The Chicago classification of esophageal motility disorders, v3.0. *Neurogastroenterol. Motil.* 27, 160–174. <https://doi.org/10.1111/nmo.12477>.
 76. Boeckstaens, G.E., Zaninotto, G., and Richter, J.E. (2014). Achalasia. *Lancet* 383, 83–93. [https://doi.org/10.1016/S0140-6736\(13\)60651-0](https://doi.org/10.1016/S0140-6736(13)60651-0).
 77. Martin-Harris, B., and Jones, B. (2008). The videofluorographic swallowing study. *Phys. Med. Rehabil. Clin. N. Am.* 19, 769–785. viii. <https://doi.org/10.1016/j.pmr.2008.06.004>.
 78. Welby, L., Caudill, H., Yitsey, G., Hamad, A., Bunyak, F., Zohn, I.E., Maynard, T., LaMantia, A.S., Mendelowitz, D., and Lever, T.E. (2020). Persistent feeding and swallowing deficits in a mouse model of 22q11.2

- p deletion syndrome.
- Front. Neurol.*
- 11, 4.
- <https://doi.org/10.3389/fneur.2020.00004>
- .
79. Mueller, M., Thompson, R., Osman, K.L., Andel, E., DeJonge, C.A., Kington, S., Stephenson, Z., Hamad, A., Bunyak, F., Nichols, N.L., et al. (2022). Impact of limb phenotype on tongue denervation atrophy, dysphagia penetrance, and survival time in a mouse model of ALS. *Dysphagia* 37, 1777–1795. <https://doi.org/10.1007/s00455-022-10442-4>.
 80. Spencer, N.J., and Hu, H. (2020). Enteric nervous system: sensory transduction, neural circuits and gastrointestinal motility. *Nat. Rev. Gastroenterol. Hepatol.* 17, 338–351. <https://doi.org/10.1038/s41575-020-0271-2>.
 81. Oh, S.W., Harris, J.A., Ng, L., Winslow, B., Cain, N., Mihalas, S., Wang, Q., Lau, C., Kuan, L., Henry, A.M., et al. (2014). A mesoscale connectome of the mouse brain. *Nature* 508, 207–214. <https://doi.org/10.1038/nature13186>.
 82. Abe, T., Kiyonari, H., Shioi, G., Inoue, K., Nakao, K., Aizawa, S., and Fujimori, T. (2011). Establishment of conditional reporter mouse lines at ROSA26 locus for live cell imaging. *Genesis* 49, 579–590. <https://doi.org/10.1002/dvg.20753>.
 83. Schindelin, J., Arganda-Carreras, I., Frise, E., Kaynig, V., Longair, M., Pietzsch, T., Preibisch, S., Rueden, C., Saalfeld, S., Schmid, B., et al. (2012). Fiji: an open-source platform for biological-image analysis. *Nat. Methods* 9, 676–682. <https://doi.org/10.1038/nmeth.2019>.
 84. Dobin, A., Davis, C.A., Schlesinger, F., Drenkow, J., Zaleski, C., Jha, S., Batut, P., Chaisson, M., and Gingeras, T.R. (2013). STAR: ultrafast universal RNA-seq aligner. *Bioinformatics* 29, 15–21. <https://doi.org/10.1093/bioinformatics/bts635>.
 85. Stuart, T., Butler, A., Hoffman, P., Hafemeister, C., Papalexi, E., Mauck, W.M., 3rd, Hao, Y., Stoeckius, M., Smibert, P., and Satija, R. (2019). Comprehensive integration of single-cell data. *Cell* 177, 1888.e21–1902.e21. <https://doi.org/10.1016/j.cell.2019.05.031>.
 86. Vong, L., Ye, C., Yang, Z., Choi, B., Chua, S., Jr., and Lowell, B.B. (2011). Leptin action on GABAergic neurons prevents obesity and reduces inhibitory tone to POMC neurons. *Neuron* 71, 142–154. <https://doi.org/10.1016/j.neuron.2011.05.028>.
 87. Madisen, L., Garner, A.R., Shimaoka, D., Chuong, A.S., Klapoetke, N.C., Li, L., van der Bourg, A., Niino, Y., Egolf, L., Monetti, C., et al. (2015). Transgenic mice for intersectional targeting of neural sensors and effectors with high specificity and performance. *Neuron* 85, 942–958. <https://doi.org/10.1016/j.neuron.2015.02.022>.
 88. Lechner, S.G., and Lewin, G.R. (2009). Peripheral sensitisation of nociceptors via G-protein-dependent potentiation of mechanotransduction currents. *J. Physiol.* 587, 3493–3503. <https://doi.org/10.1113/jphysiol.2009.175059>.
 89. Hernandez-Miranda, L.R., Ruffault, P.L., Bouvier, J.C., Murray, A.J., Morin-Surun, M.P., Zampieri, N., Cholewa-Waclaw, J.B., Ey, E., Brunet, J.F., Champagnat, J., et al. (2017). Genetic identification of a hindbrain nucleus essential for innate vocalization. *Proc. Natl. Acad. Sci. USA* 114, 8095–8100. <https://doi.org/10.1073/pnas.1702893114>.
 90. Hörl, D., Rojas Rusak, F., Preusser, F., Tillberg, P., Randel, N., Chhetri, R.K., Cardona, A., Keller, P.J., Harz, H., Leonhardt, H., et al. (2019). BigStitcher: reconstructing high-resolution image datasets of cleared and expanded samples. *Nat. Methods* 16, 870–874. <https://doi.org/10.1038/s41592-019-0501-0>.
 91. Wefers, B., Bashir, S., Rossius, J., Wurst, W., and Kühn, R. (2017). Gene editing in mouse zygotes using the CRISPR/Cas9 system. *Methods* 121–122, 55–67. <https://doi.org/10.1016/j.ymeth.2017.02.008>.
 92. Walcher, J., Ojeda-Alonso, J., Haseleu, J., Oosthuizen, M.K., Rowe, A.H., Bennett, N.C., and Lewin, G.R. (2018). Specialized mechanoreceptor systems in rodent glabrous skin. *J. Physiol.* 596, 4995–5016. <https://doi.org/10.1113/JP276608>.

STAR★METHODS

KEY RESOURCES TABLE

| REAGENT or RESOURCE | SOURCE | IDENTIFIER |
|--|-------------------------|---|
| Antibodies | | |
| Chicken polyclonal anti-GFP | Aves Labs | Cat#: GFP-1020; RRID:AB_10000240 |
| Rat monoclonal anti-GFP | Nacalai Tesque | Cat#: GF090R; RRID:AB_2314545 |
| Rabbit polyclonal anti-RFP | Rockland | Cat#: 600-401-379-RTU; RRID:AB_2209751 |
| Goat polyclonal anti-Phox2b | R&D Systems | Cat#: AF4940; RRID:AB_10889846 |
| Sheep polyclonal anti-TH | Millipore | Cat#: AB1542; RRID:AB_90755 |
| Rabbit monoclonal anti-Pou3f1 | Abcam | Cat#: ab126746; RRID:AB_11130256 |
| Goat polyclonal anti-ChAT | Millipore | Cat#: AB144P; RRID:AB_2079751 |
| Goat polyclonal anti-c-Kit | R&D Systems | Cat#: AF1356; RRID:AB_354750 |
| Goat polyclonal anti-CTb | List Labs | Cat#: 703; RRID:AB_10013220 |
| Rabbit polyclonal anti-Tubb3 | BioLegend | Cat#: Poly18020; RRID:AB_2564645 |
| Rat monoclonal anti-CK8 | DSHB | Cat#: TROMA-I; RRID:AB_531826 |
| Mouse monoclonal anti-SMA | Sigma | Cat#: A2547; RRID:AB_476701 |
| Guinea Pig Polyclonal Anti-CGRP | Synaptic Systems | Cat#: 414004; RRID:AB_2737049 |
| Rabbit polyclonal anti-CD31 | Abcam | Cat#: Ab28364; RRID:AB_726362 |
| Bacterial and virus strains | | |
| AAV9-FLEX-tdTomato | Oh et al. ⁸¹ | RRID:Addgene_#51503 |
| Chemicals, peptides, and recombinant proteins | | |
| Opal 520 | Akoya Biosciences | Cat#: FP1487001KT |
| Opal 570 | Akoya Biosciences | Cat#: FP1488001KT |
| Opal 650 | Akoya Biosciences | Cat#: FP1496001KT |
| 405M Tyramide | Biotium | Cat#: 96057 |
| Urea 98% | Acros Organics | N/A |
| Quadrol | Sigma | Cat#: 122262 |
| Triton X-100 | Sigma | Cat#: X100 |
| EasyIndex RI=1.46 | LifeCanvas Technologies | N/A |
| Critical commercial assays | | |
| RNAscope Fluorescent Multiplex Reagent Kit | ACD | Cat#: 323110 |
| Agilent RNA Pico Kit | Agilent | Cat#: 5067-1513 |
| Agilent High Sensitivity DNA Kit | Agilent | Cat#: 5067-4626 |
| MEGAscript T7 Transcription Kit | Ambion | Cat#: AM1334 |

(Continued on next page)

Continued

| REAGENT or RESOURCE | SOURCE | IDENTIFIER |
|---|---------------------------------|---|
| Deposited data | | |
| Single cell RNA-sequencing | Gene Expression Omnibus | GEO: GSE206052 |
| Experimental models: Organisms/strains | | |
| Mouse: VGlut2 ^{Cre} | Jackson Laboratory | RRID:IMSR_JAX:016963 |
| Mouse: R26 ^{nGFP} | Abe et al. ⁸² | N/A |
| Mouse: Prox2 ^{FlpO} | This paper | N/A |
| Mouse: Runx3 ^{Cre} | Levanon et al. ⁴⁵ | N/A |
| Mouse: Ai65 | Jackson Laboratory | RRID:IMSR_JAX:021875 |
| Mouse: Ai80 | Jackson Laboratory | RRID:IMSR_JAX:025109 |
| Mouse: Phox2b ^{Cre} | D'Autréaux et al. ³⁶ | N/A |
| Mouse: Oxt ^{T2A-Cre} | Jackson Laboratory | RRID:IMSR_JAX:031303 |
| Mouse: R26 ^{FTLG} | Dempsey et al. ⁴⁸ | N/A |
| Mouse: Tau ^{ds-DTR} | Britz et al. ⁶² | N/A |
| Oligonucleotides | | |
| Mm-Prox2-C3 | ACD | Cat#: 593331-C3 |
| Mm-Runx3 | ACD | Cat#: 451271 |
| Mm-Phox2b-C2 | ACD | Cat#: 407861-C2 |
| Mm-Phox2b-C3 | ACD | Cat#: 407861-C3 |
| Mm-Runx3-C2 | ACD | Cat#: 451271-C2 |
| Mm-Piezo2-C2 | ACD | Cat#: 400191-C2 |
| Mm-Piezo2-C3 | ACD | Cat#: 400191-C3 |
| Mm-Gata3 | ACD | Cat#: 403321 |
| Mm-Rbp4-C2 | ACD | Cat#: 508501-C2 |
| Mm-Grm5-C2 | ACD | Cat#: 423631-C2 |
| Mm-Mc4r | ACD | Cat#: 319181 |
| Mm-Lamp5-C2 | ACD | Cat#: 451071-C2 |
| Mm-Gabrg1-C3 | ACD | Cat#: 501401-C3 |
| Mm-Slc18a3-C3 | ACD | Cat#: 448771-C3 |
| Mm-Calb1-C3 | ACD | Cat#: 428431-C3 |
| Mm-Adra2a-C3 | ACD | Cat#: 425341-C3 |
| Mm-VGlut2-C3 | ACD | Cat#: 319171-C3 |
| Mm-Prrxl1 | ACD | Cat#: 446631 |
| Mm-Trpv1 | ACD | Cat#: 313331 |
| Mm-Glp1r | ACD | Cat#: 418851 |
| Mm-Oxtr | ACD | Cat#: 412171 |
| Recombinant DNA | | |
| Prox2FlpO targeting vector | GeneArt Invitrogen | Cat#: 817007DE |
| Software and algorithms | | |
| FIJI | Schindelin et al. ⁸³ | RRID:SCR_002285 |
| PRISM 6 | GraphPad | RRID:SCR_002798 |
| Adobe Illustrator CS6 | Adobe | RRID:SCR_010279 |
| Drop-Seq Tools v2.0 | Broad Institute | https://github.com/broadinstitute/Drop-seq |
| Picard Tools v2.18.17 | Broad Institute | RRID:SCR_006525 |
| STAR v2.5.3a | Dobin et al. ⁸⁴ | https://github.com/alexdobin/STAR |
| Seurat v3.0 | Stuart et al. ⁸⁵ | RRID: SCR_007322 |

RESOURCE AVAILABILITY

Lead contact

Further information and requests for resources and reagents should be directed to and will be fulfilled by the lead contact, Carmen Birchmeier (cbirch@mdc-berlin.de).

Materials availability

All unique reagents generated in this study are available from the [lead contact](#) with a completed materials transfer agreement.

Data and code availability

- The next-generation sequencing datasets generated in this study have been deposited in the GEO repository (GEO accession number GSE206052) and are publicly available.
- This paper does not report original code.
- Any additional information required to reanalyze the data reported in this work paper is available from the [lead contact](#) upon request.

EXPERIMENTAL MODEL AND SUBJECT DETAILS

Mouse lines

All experiments were conducted according to regulations established by the Max Delbrück Centre for Molecular Medicine, LAGeSo (Landesamt für Gesundheit und Soziales), the institutional animal care and use committee at the University of Missouri, and the institutional animal care and use committee at Harvard Medical School. *Ai65* (#021875), *Ai80* (#025109), *VGlut2^{Cre}* (#016963), and *Oxt^{T2A-Cre}* mice were obtained from the Jackson Laboratory.^{59,86,87} *Phox2b^{Cre}*,³⁶ and *R26^{FTLG}* mice⁴⁸ were provided by Jean-François Brunet (Institut de Biologie de l'ENS, Paris, France). The *Tau^{ds-DTR}* and *Runx3^{Cre}* mice were provided by Martyn Goulding (Salk Institute) and Yoram Groner (Weizmann Institute, Rehovot, Israel).^{45,62} The *Gt(ROSA)26Sor^{tm2.1Sia}* mice were provided by Shinichi Aizawa (RIKEN Center for Developmental Biology); we refer to them as *R26^{nGFP}* mice, as they express a nuclear GFP upon cre-mediated stop cassette excision.⁸² Mice were housed at defined room temperature (23°C), humidity (56%), and with a 12-hour light-dark cycle. Male and female mice were used in approximately equal numbers for all experiment in this study unless otherwise noted.

METHOD DETAILS

Vagal neuron isolation

We dissected the vagal ganglia from 15 *VGlut2^{Cre};R26^{nGFP}* mice of either sex at P4, removed excess nerve, muscle and vascular tissue, and placed them in a 1.5 ml Eppendorf tube with warm F12/FHS (F12 with 10% fetal horse serum). Neurons were isolated essentially as described.⁸⁸ In short, ganglia were digested in F12/FHS solution containing 0.125% collagenase, incubated at 37°C for 1 hour, washed 3x in PBS, and then incubated in PBS with 0.25% trypsin at 37°C for 15 minutes. Dissociation of the ganglia was performed using fire-polished Pasteur pipettes of decreasing diameter. The solution was transferred on top of a 2 ml BSA cushion (F12/FHS solution with 15% bovine serum albumin) and spun for 10 minutes at 900 RPM. The cell pellet was resuspended in 500 µl of HBSS without calcium or magnesium, strained twice through a 70 µm filter (Sysmex), and DAPI (Sigma) was added to a final concentration of 300 nM to label dead cells before sorting. We sorted GFP-positive/DAPI-negative cells into 96-well plates using ARIA Sorter III (BD) and BD FACSDiva software 8.0.1.

Library generation and sequencing

Single cell RNA sequencing was done following the CEL-Seq2 protocol.³¹ cDNA Libraries were prepared for 16 96-well plates, pooled together, and sequenced on a NextSeq 500 (Illumina) in two separate runs by the next generation sequencing core facility of the Max-Delbrück Center for Molecular Medicine.

Analysis of the P4 vagal ganglia CEL-Seq2 data

Data processing and gene quantification was performed using dropseq-tools v2.0 and picard-tools v2.18.17. We used the standard pipeline for Drop-seq data, with the necessary adaptations to analyze the CEL-Seq2 data. We removed the bead barcode correction steps, and in the DigitalExpression quantification we inputted the list of 96 CEL-Seq2 barcodes. Alignment was performed with STAR v2.5.3a. We used the GRCh38 genome and the annotation from the GRCh38.p4 assembly. Two thresholds were set to filter out wells without cells or wells with multiple cells. We set a lower threshold of 17,000 UMIs (unique molecular identifier) per cell, and an upper threshold of 250,000 UMIs per cell. These UMI thresholds filtered out 144 cells, leaving 1392 out of 1536 cells (from 16 96-well plates), e.g. 9.4% of the total cell count were removed from further analysis.

Downstream analysis was performed with Seurat v3.0. Seurat was run with the default parameters with the following exceptions. 2000 genes were selected with the FindVariableFeatures function of Seurat. The first 30 principal components were selected after

PCA, excluding PC3 and PC11 as these PCs represented glial contamination in our dataset. The neighbor graph was constructed with FindNeighbors with a k parameter of 11. The clustering resolution was set to 1. UMAP visualization was used with the correlation metric and 20 number of neighbors.

Integration analysis

For the integration analysis the raw count tables were used from the Ernfor and Knight laboratories.^{10,11} The first was downloaded from a public repository and the second was kindly provided by the authors. The Bai et al. data consisted of two datasets, the targeted and the untargeted cells, which were sequenced with different protocols.¹⁰ Seurat v3.0 canonical correlation was used to integrate the four datasets (including ours), using 30 canonical components. Initially, PCA was performed for 30 principal components. The neighbor graph was constructed with those 30 components, with a k parameter of 20, and clustering was performed with a resolution of 1. After this initial analysis we identified clusters of glial and epithelial cells and sympathetic neurons. We then removed these cell clusters and repeated the integration analysis on the remaining cells. This time integration was performed using 40 canonical components. After PCA, the first 29 components were used, excluding principal components 4 and 6 as these carried a glial signal. The rest of the downstream integration analysis was performed using default parameters.

Tissue preparation

Mice were sacrificed and perfused with PBS before organ harvesting. Dissected organs were washed in PBS before fixation in 4% PFA in PBS (1 hour for vagal ganglia, 4 hours for digestive organs and 6 hours for brains). After fixation, organs were washed in PBS, cryopreserved in 15% sucrose overnight at 4°C, and then in 30% sucrose overnight at 4°C. Organs were embedded with Tissue-Tek O.C.T Compound (Sakura) and stored at -80°C until cryosectioning. Vagal ganglia were cryosectioned at 16µm, whereas digestive organs and brains were cryosectioned at 30µm. Sections were stored at -80°C until used.

Single molecule fluorescent *in situ* hybridization (RNAscope) and immunohistology

In situ fluorescent hybridization was performed using the RNAscope Multiplex Fluorescent Reagent Kit V2 from ACDbio according to the manufacturer's instructions. Briefly, vagal ganglia sections were thawed at 37°C for 30 minutes and post-fixed in 4% PFA in PBS for 15 minutes before washing in PBS and continuing with the manufacturer's instructions. To combine immunohistology with RNAscope, the instructions were followed up to the hydrogen peroxide wash, then the sections were washed in PBS and incubated at 4°C overnight with the primary antibody diluted in Co-Detection Antibody Diluent (obtained from ACDBio). The sections were washed in PBS and treated with Protease III. The RNAscope protocol was then continued, the sections washed in PBS and incubated with the secondary antibody for 1 hour at room temperature in blocking solution (PBS with 0.2% Triton X-100 and 5% normal horse serum). Sections were washed in PBS and mounted with ProLong Gold Antifade mountant (ThermoFisher). We used the following probes in this study: Prox2 (593331-C3), Runx3 (451271 and 451271-C2), Piezo2 (400191-C2 and 400191-C3), Trpv1 (313331), Prrxl1 (446631), Calb1 (428431-C3), Adra2a (425341-C3), Slc18a3 (448771-C3), Slc17a6 (319171-C3), Phox2b (407861-C2 and 407861-C3), Rbp4 (508501-C2), Gata3 (403321), Grm5 (423631-C2), Lamp5 (451071-C2), Mc4r (319181), Gabrg1 (501401-C3), Oxt (412171) and Glpr (418851).

Immunohistology was performed as described with minor modifications.⁸⁹ In short, sections were thawed, briefly washed (PBS with 0.2% Triton X-100), and blocked (PBS with 0.2% Triton X-100 and 5% normal horse serum) for 1 hour at room temperature. The primary antibody was diluted in blocking solution and incubated for 1-2 days at room temperature. Sections were washed in PBS before being incubated with the secondary antibody diluted in blocking solution for 1 hour at room temperature. Sections were again washed in PBS and mounted with Immu-Mount (ThermoFisher). The following primary antibodies were used: goat anti-Phox2b (R&D Systems, AF4940, 1:200), rabbit anti-RFP (Rockland, 600-401-379-RTU, 1:500), chicken anti-GFP (Aves Labs, GFP-1020, 1:500), rat anti-GFP (Nacalai Tesque, GF090R, 1:1000), goat anti-CD117 (R&D Systems, AF1356, 1:400), rabbit anti-Tubulin β -3 (BioLegend, Poly18020, 1:1000), goat anti-CTb (List Labs, 703, 1:2000), rabbit anti-Pou3f1 (Abcam, ab126746, 1:500), sheep anti-TH (Millipore, AB1542, 1:1000), goat anti-ChAT (Millipore, AB144P, 1:200), rat anti-CK8 (DSHB, TROMA-I, 1:400), mouse anti-SMA (Sigma, A2547, 1:2000), guinea pig anti-CGRP (Synaptic Systems, 414004, 1:1000) and rabbit anti-CD31 (abcam, Ab28364, 1:500). We used species specific secondary antibodies coupled to Cy2-, Cy3- and Cy5 (Jackson ImmunoResearch, 1:500). After immunostaining or smFISH, tissue sections were imaged using an LSM 700 confocal microscope (Carl Zeiss) with ZEN 2012 software. When images were acquired using the tile-scan modus, this is mentioned in the corresponding figure legends.

Whole organ immunohistology and clearing

Mice were sacrificed, perfused with PBS to remove the blood and then perfused with 4% PFA in PBS. Vagal ganglia and digestive organs were dissected and fixed overnight at 4°C in 4% PFA in PBS. Tissue was cleared using the CUBIC protocol.⁴⁹ Briefly, tissue was first washed overnight at room temperature in PBS and then immersed in ScaleCUBIC-1 (a mixture of 25% urea, 25% Quadrol, 15% Triton X-100 and 35% MQ-H₂O) diluted 1:1 with MQ-H₂O overnight in a 37°C water bath. The tissue was then placed in ScaleCUBIC-1 in a 37°C water bath until the tissue became transparent (1/2 a day for vagal ganglia and 2-4 days for digestive organs). The solution was exchanged every 2 days. Once the organs were sufficiently cleared they were washed overnight at room temperature in PBS + 0.2% Triton X-100. Next, we incubated the organs with the primary antibodies diluted in modified blocking solution (PBS with 10% Triton X-100, 5% normal horse serum and 300mM NaCl) for 10 days on a shaker at 37°C, refreshing the antibodies

after 5 days. Organs were washed overnight in PBS with 0.2% Triton X-100, incubated with the secondary antibodies and DAPI in modified blocking solution for 8 days on a shaker at 37°C, refreshing the antibodies after 4 days. The tissue was then immersed in EasyIndex RI=1.46 (LifeCanvas Technologies) diluted 1:1 with MQ-H₂O overnight in a 37°C water bath, before being transferred to EasyIndex RI=1.46 overnight for the final refraction index matching. Once the tissue was cleared, stained and refractive index matched it was placed into a square plastic mold filled with a 2% low melting point agarose prepared with EasyIndex RI=1.46.

Cleared ganglia were imaged using a Zeiss lightsheet 7 microscope, while cleared digestive organs were imaged using a custom built mesoSPIM microscope.⁵⁰ Cleared, stained and embedded digestive organs were immersed in EasyIndex RI=1.46 inside a small quartz glass cuvette (45 x 12.5 x 22.5 mm Portmann Instruments AG, UQ-205, quartz glass), which was placed inside a larger chamber (40 x 40 x 100 mm, Portmann Instruments AG, UQ-753-H100) filled with RI-matching liquid for fused silica (RI=1.46, Cargille Cat. #19569). The lightsheet illumination was delivered sequentially from the left and right sides, resulting in two different stacks per view, which were registered and fused into a single stack using BigStitcher⁹⁰ for each channel. The excitation laser line (Hübner Photonics C-Flex: 561 nm) was used with the corresponding detection filter (Chroma ET590/50m). The esophagus/stomach from an 3-months-old *Prox2^{FlpO};Phox2b^{Cre};Ai65 (Prox2/Runx3^{Tom})* mouse was acquired with a 1 x 3 tile scan at 1x zoom, while the esophagus/stomach from a 3-months-old *Runx3^{Cre};Prox2^{FlpO};Ai65 (Runx3^{Tom})* mouse was acquired with a 2 x 6 tile scan at 2x zoom (Olympus 1x MVPLAPO1x). The images displayed in Figure 2A are maximum intensity Z-projections of the final fused images. Vagal neuron counts at P4 were performed with Imaris v9.9.

Retrograde tracing

CTb tracing from the abdominal esophagus and stomach

WT adult mice (~3 month of age) were anesthetized with an intraperitoneal injection of ketamine/xylazine (80 mg/kg body weight ketamine and 10 mg/kg body weight xylazine). The abdomen was shaved and betadine was applied to the abdominal skin. Ophthalmic ointment was applied to the eyes to prevent them from drying out during the procedure. A small transverse laparotomy was made below the sternum and fire polished glass Pasteur pipettes were used to position the organs prior to injection. Glass injection needles were prepared with a DMZ universal electrode puller (Zeitz-Instruments) and filled with 0.5% CTb solution (ThermoFisher) in 0.9% NaCl. We added 0.2% Fast Green (Sigma) to visualize the injection site and to confirm a successful injection. For glandular and non-glandular stomach injections, a total of 2 μ l was injected, while for abdominal esophagus 1 μ l was injected, due to the smaller size of the target region. The injections were performed using a Nanoject III Programmable Nanoliter Injector (Drummond Scientific Company), with a volume of 250 nl and a speed of 50 nl/s per injection. In all cases, the needle was carefully placed into the muscle layer of the target regions and allowed to remain in place for 10 s before and after each injection. After the injections, we performed layered wound closure, suturing the abdominal muscle layer first, followed by suturing the skin. Post-surgery mice were given a subcutaneous injection of Carprofen (5 mg/kg body weight) and received Metamizol 1 ml/100 ml drinking water for analgesia. Mice were monitored twice daily to ensure that they were recovering properly, then were euthanized 4-5 days following surgery for harvesting of vagal ganglia.

Fast Blue tracing from the cervical and thoracic esophagus

We first measured the length of the esophagus in P7 WT mice and found that it measured around 2 cm from the base of the tongue to the stomach. Next, we prepared a 0.25% Fast Blue solution in 50% 0.9% NaCl and 50% glycerol. To trace from the cervical and thoracic esophagus, mice were gavaged 2 times with 2 μ l of the Fast Blue solution 0.5 cm and 1.3 cm from the base of the tongue, respectively. Animals were monitored twice daily and were euthanized 7 days following Fast Blue gavage.

Anterograde tracing

AAV injections into the vagal ganglia were done as reported previously,¹² with minor modifications. The vagal ganglia were surgically exposed and serially injected (50 x 20 nl) with AAV solution containing 0.05% Fast Green FCF Dye (Sigma) using a Nanoject III Injector (Drummond). AAV solutions: AAV-*flex-tdTomato* solution was AAV9.CAG.Flex.tdTomato.WPRE.BGH (Addgene viral prep #51503-AAV9, ~10¹³ genome copies/ml). Animals recovered from surgery and were sacrificed 4 weeks later for histology. Mice were sacrificed, perfused with PBS to remove the blood, and the esophagus was fixed overnight in 4% PFA. The ganglia were examined for endogenous tdTomato signal to establish efficiency and specificity of the injection. The esophagus was then washed in PBS three times and transferred to PBS overnight. A muscle layer peel from the esophagus was obtained by carefully separating the muscle layer from the underlying mucosal layer using fine forceps. The muscle layer of the esophagus was blocked (PBS, 5% donkey serum, 0.1% Triton X-100) overnight at 4°C. The tissue was stained for tdTomato as previously described except antibody incubations were 3-4 days and washes with PBST (PBS, 0.1% Triton X-100) were at least 3x12 hours, 4°C. The tissue was then mounted within a silicon slide gasket and the muscle peel was flattened between the slide and coverslip for optimal whole-mount imaging. Fluorescence signal was captured on a Leica SP5 II confocal microscope, analyzed in FIJI, and the final images displayed in Figure 3G are maximum intensity Z-projections.

Generation of *Prox2^{FlpO}* mice

Prox2^{FlpO} mice were generated at the transgenic core facility at the Max Delbrück Center for Molecular Medicine in Berlin using CRISPR/Cas9 to insert a 1.5kb fragment containing the codon-optimized FLP recombinase (FlpO) and a bovine poly(A) sequence between the 5' UTR and 1st exon of the *Prox2* gene by homology-directed repair.⁹¹ The donor vector was synthesized by

GeneArt (Invitrogen GeneArt, ThermoFisher), and contained genomic sequences 2kb upstream (5' homology arm) and 2kb downstream (3' homology arm) of the 1st exon of the *Prox2* gene. The successful insertion of the vector was confirmed by long range PCR. *Prox2^{FlpO}* mice were born at the correct Mendelian ratios, and could not be distinguished from wild-type littermates based on their appearance, behavior, fertility or lifespan. See also reference Nishijima and Ohtoshi.⁴⁰

Esophagus and stomach single fiber nerve recordings and analysis

Electrophysiological single fiber nerve recordings were realized using an *ex-vivo* esophagus/stomach vagal nerve preparation.⁶⁰ Briefly, adult *Prox2/Runx3^{ChR}* (*Prox2^{FlpO};Phox2b^{Cre};Ai80*) mice were sacrificed by CO₂ euthanasia. Mice were transcardially perfused (40 ml) with a carbogen equilibrated extracellular solution (125 mM NaCl, 2.5 mM KCl, 25 mM NaHCO₃, 1.25 mM NaH₂PO₄, 1 mM MgCl₂, 2 mM CaCl₂, 20 mM glucose and 20 mM HEPES). The entire esophagus or stomach was pinned in a dissection chamber with flowing equilibrated extracellular solution (20–23°C), with the attached vagus nerve that was isolated from the cervical to the thoracic esophagus (esophagus analysis) or from the cervical esophagus to the lower esophageal sphincter (stomach analysis). For the esophagus analysis, an open-book preparation was obtained by sectioning the esophagus longitudinally, taking care not to damage lateral ramifications of the vagus nerve. Esophageal recordings were made by probing the thoracic to abdominal esophagus. For the stomach preparation, the esophagus was removed at the lower esophageal sphincter, and the intestine was removed 1.5–2 cm distal to the pyloric sphincter. A cannula (0.63 mm diameter) connected to a 1 ml syringe filled with fresh extracellular solution was inserted into the intestine and secured in place with a suture. A small hole was perforated in the forestomach with a 0.8 mm gauge needle to allow for pressure equilibration after stomach distension. The preparation was then transferred to a recording chamber perfused with warm (32°C) carbogen saturated extracellular solution, and the vagus nerve was passed through a channel to an adjacent recording chamber containing mineral oil. Small nerve bundles were teased apart and placed on a platinum recording electrode.

In the esophagus and stomach, mechanosensitive fibers were identified by manually poking the tissue in the recording chamber, and tested for their *Prox2/Runx3* identity using optogenetic stimulation (470 nm Thorlab diode laser, 1 second stimulation, intensity 2 mW/mm²) delivered by a 1 mm fiber optic placed on the responsive field. After observing a light-sensitive response, mechanosensitive esophageal fiber characterization was performed using a piezo actuator (Physik Instrumente, Germany, P-602.508) connected to a force measurement device (Kleindiek Nanotechnik, Reutlingen, Germany, PL-FMS-LS).⁹² Different mechanical forces (ranging from 50 mN to 250 mN) were applied with a 2 sec static phase. We allowed fibers to recover for 1 min before applying the next stimulation. For analysis of stomach mechanosensitive fibers, we applied increasing volumes (0.1, 0.2, 0.3 ml) to distend the entire stomach, allowing pressure equilibration by removing the added liquid and waiting 5 minutes between each distension. Stomach distention was continuously recorded via a force measurement device connected to a 1 mm probe placed on the ventral wall of the stomach.

Raw data were recorded using an analog output from a Neurolog amplifier, filtered (100–5 kHz) and digitized (10 kHz) using a Powerlab 4/30 system and Labchart 8 software with the spike-histogram extension (ADInstruments Ltd., Dunedin, New Zealand). Single nerve fiber recordings were further analyzed to identify single units using Spike2 software (ced.co, Spikes2 version 10). Individual spike units were identified based on the following parameters: new template width as % of amplitude: 32, minimum % of points in template: 60, minimum occurrence of events: 1/50, spike duration considered for the sorting -1.5 to 1.5 ms. Unit spikes were binned per 200 ms to ease data analysis and light/mechanosensitive and -insensitive units were separated. For each fiber recording, between 3–10 separate mechanosensitive units were identified. To be categorized as *Prox2/Runx3*-positive, the unit had to increase its firing at least 2-fold during light stimulation. For each preparation, between 4–7 light stimulations were performed. To be considered *Prox2/Runx3*-positive, units had to respond to at least 60% of the stimuli.

Firing patterns were further analyzed using Microsoft Excel. *Prox2/Runx3*-positive and -negative units were aligned using the onset of the mechanical stimuli, and activities of individual units were normalized using the basic activity measure of the unit 2 seconds before the stimulus onset to obtain the Δ Frequency (Hz). For population quantifications, mechanosensitive, light sensitive, and mech- and light sensitive units were binned, and the unit activity observed 1 second after the onset of the stimuli was averaged. *Prox2/Runx3*-positive fibers were manually decomposed depending on their firing pattern during either the 300 mN mechanical or the 0.3 ml stomach distention. Two types of firing responses were observed, which were separately binned using a firing decay of 40% 1 second after the stimulus onset as criterion. Type I units displayed a prolonged firing pattern with a slower decay, i.e. the units continued to spike until the offset of the mechanical stimuli (slowly adapting). Type II units displayed a fast decay after the stimulus onset, and rapidly returned to basal activity before the end of the stimuli (rapidly adapting).

Ablation

We generated *Prox2/Runx3^{ds-DTR}* (*Prox2^{FlpO};Phox2b^{Cre};Tau^{ds-DTR}*) mice in which all cells with a history of *Phox2b* and *Prox2* expression expressed the human diphtheria toxin receptor. We ablated *Prox2/Runx3* vagal neurons in adult mice (~6 months of age) by i.p. injection of Diphtheria toxin (DT, Sigma), reconstituted in 0.9% NaCl, and injected at a concentration of 40 ng/g bodyweight. After DT administration the ablation mice were monitored twice daily. If their weight dropped below 10% of their starting weight, they received a 0.5 ml i.p. injection of 0.9% NaCl daily and were given access to a nutritionally fortified water gel (DietGel Recovery from ClearH₂O). One male mouse continued to lose weight after the ablation and was euthanized before it could undergo endline testing. All other mice stabilized between 5–7 days post ablation.

Behavior

Videofluoroscopy experiments to measure *in vivo* swallowing function were performed as previously described.^{28,78} Briefly, mice (n=15, 8M and 7F, genotype: *Prox2^{FipO};Phox2b^{Cre};Tau^{ds-DTR}*, 6 months of age) underwent videofluoroscopy swallow study (VFSS) at the University of Missouri using customized equipment and analysis software. The mice were shipped from the Max Delbrück Center in Berlin, Germany to the University of Missouri in MO, USA and were placed in quarantine for 3 weeks. During this time the mice were behaviorally conditioned with the VFSS chamber and oral contrast solution in order to familiarize them with the experimental set up and facilitate drinking during VFSS testing. Following release from quarantine, the mice were water restricted overnight for 12 hours in order to increase their motivation to drink during testing the following morning. During the water restriction period, a VFSS chamber was placed in each home cage. Mice were each tested in their respective home cage chambers the following morning. VFSS testing was performed individually using a miniaturized, low energy (30 kV, 0.2 mA) fluoroscope (The LabScope, Glenbrook Technologies, Newark, NJ, USA) and videos were captured at 30 frames per second. Mice were gently placed into the VFSS chamber and enclosed using two end-caps. One end-cap had a small bowl attached through which the liquid contrast agent (Omnipaque, GE Healthcare, 350 mg iodine/ml; diluted to a 25% solution with deionized water and 3% chocolate flavoring) could be administered during testing. The test chamber was then positioned within the lateral plane of the fluoroscope, and the bowl was filled with the liquid contrast agent via a custom syringe delivery device. When the mice began to drink, the fluoroscope was activated via a foot pedal. In order to minimize the radiation exposure time, the fluoroscope was turned off when the mice turned away from the bowl or initiated non-drinking behaviors. If mice did not drink, we placed them back in their home cage for ~30 mins and re-tested them. We captured drinking bouts in videos of approximately 30-60 s duration and saved them as AVI files. After baseline behavioral testing, mice underwent DT ablation of *Prox2+* and *Runx3+* vagal neurons. We allowed the mice to recover for 19 days after the ablation, at which point we re-tested the mice using the same VFSS protocol. Thus, we compared the swallowing behavior of the same mice at baseline (pre-DT ablation) versus endline (post-DT ablation).

We imported the AVI files into Pinnacle Studio (version 24; Pinnacle Systems, Inc., Mountain View, CA) and identified drinking bouts between 2-5 seconds in length to obtain a total of 3-15 seconds of uninterrupted drinking per mouse. The start of the drinking bouts was always at a swallow event, defined as when the liquid bolus abruptly moved from the vallecular space to the esophagus. The 2-5 second video clips were then imported into a custom VFSS analysis software (JawTrack™, University of Missouri) for subsequent frame by frame analysis. The software allows for the semi-automated extraction of many swallowing parameters such as lick rate (number of jaw open/close cycles per second, calculated for 2-5 second long video clips and then averaged), lick interval (time between successive lick cycles throughout a 2-5 second long video clip, and then averaged), swallow rate (number of swallows in each second of a 2-5 second video clip, then averaged), swallow interval (time between successive swallows throughout a 2-5 second video clip, then averaged), lick-swallow ratio (number of jaw open/close cycles between each successive swallow pair throughout a 2-5 second video clip, then averaged), pharyngeal transit time (bolus travel time through the pharynx for each swallow, then averaged), esophageal transit time (bolus travel time through the esophagus, then averaged), jaw closing velocity (speed at which the jaw closes during each jaw cycle throughout a 2-5 second video clip, then averaged) and jaw opening velocity (speed at which the jaw opens during each jaw cycle throughout a 2-5 second video clip, then averaged).^{78,79}

QUANTIFICATION AND STATISTICAL ANALYSIS

All details regarding the number of samples and statistical tests performed can be found in the figure legends. Cell quantifications were performed in a non-blind, semi-automated manner on non-consecutive sections using FIJI/ImageJ (2.3.0/1.53q). Briefly between 3-8 images per animal were imported into ImageJ and immunofluorescent stainings were counted automatically. For the smFISH experiments a tdTomato+ cell or nGFP+ nucleus had to have at least 5 dots in order to be considered positive for a particular RNAscope probe. Cells and nuclei positive for an RNAscope probe were counted manually. All paired and unpaired t-tests were two-tailed, and no statistical test was done to predetermine sample sizes. One animal (#5697) was removed as an outlier from the Swallow interval and Lick to swallow ratio plots (Figure S7C), as it failed the Grubbs' test with $\alpha=0.01$. Significance for t-tests and ANOVAs was defined as * $p < 0.05$, ** $p < 0.01$, *** $p < 0.001$, **** $p < 0.0001$. Statistical analyses were performed using GraphPad Prism v6.0c.

Supplemental information

**Prox2 and Runx3 vagal sensory neurons
regulate esophageal motility**

Elijah D. Lowenstein, Pierre-Louis Ruffault, Aristotelis Misios, Kate L. Osman, Huimin Li, Rachel S. Greenberg, Rebecca Thompson, Kun Song, Stephan Dietrich, Xun Li, Nikita Vladimirov, Andrew Woehler, Jean-François Brunet, Niccolò Zampieri, Ralf Kühn, Stephen D. Liberles, Shiqi Jia, Gary R. Lewin, Nikolaus Rajewsky, Teresa E. Lever, and Carmen Birchmeier

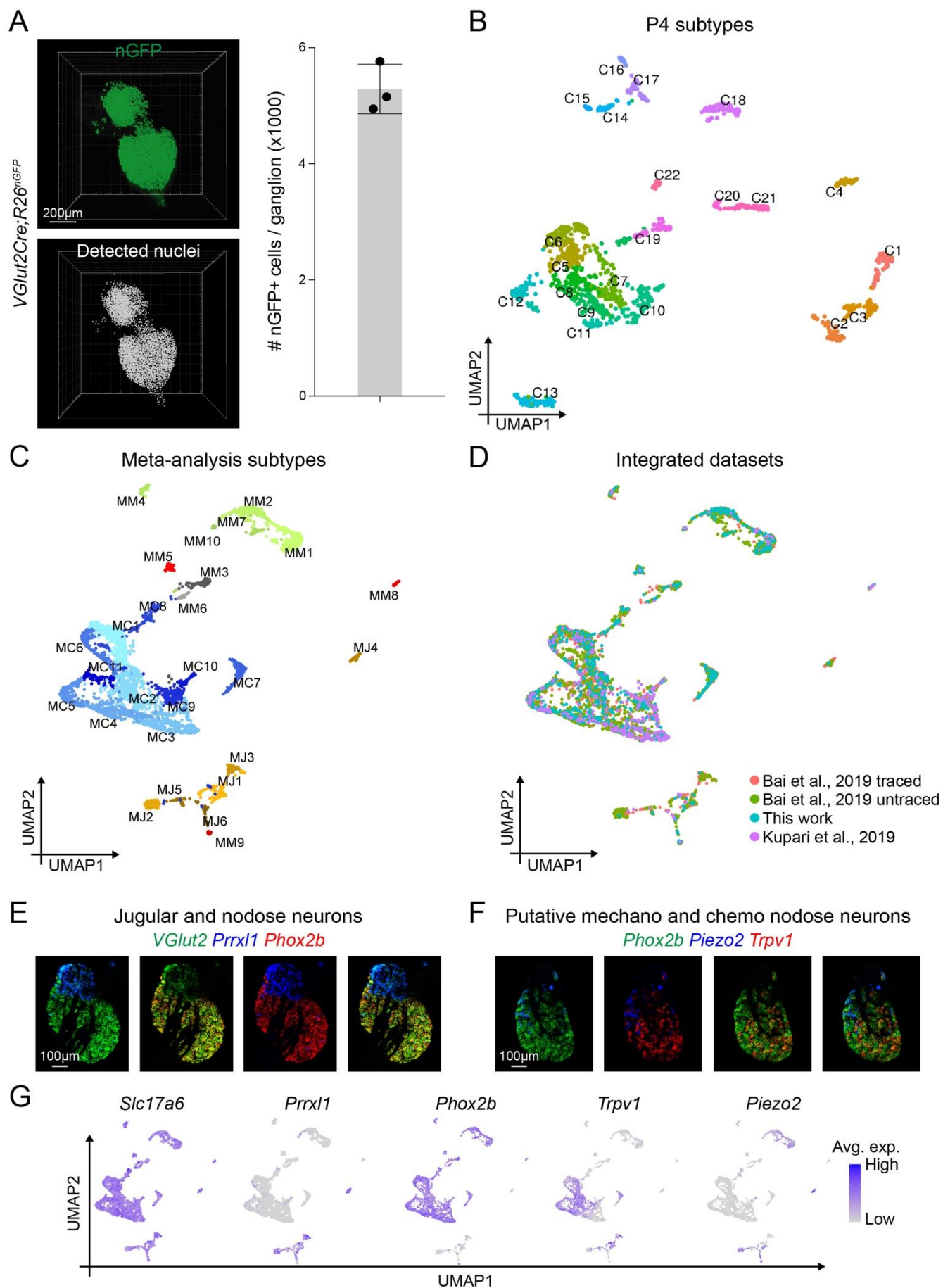


Figure S1. scRNAseq analysis assigns a developmental origin and putative function to vagal neuron subtypes, related to Figure 1. (A) Lightsheet imaging of a vagal ganglion from a *VGlut2^{Cre};R26^{nGFP}* mouse at P4; GFP+ neuronal nuclei (green, **top**), and all detected nuclei (gray, **bottom**) are shown. Detected nuclei were quantified using IMARIS v9.9.0 (5288±423 nuclei per ganglion, n=3). **(B)** UMAP plot based on single cell RNA-seq data from 1392 neurons isolated at P4 from *VGlut2^{Cre};R26^{nGFP}* animals revealed 22 subtypes (color coded and numbered). **(C)** UMAP plot based on the meta-analysis of 4,442 neurons revealed 27 subtypes (color coded and numbered, *Meta-Jugular* (MJ) 1-6, *Meta-Chemo* (MC) 1-11, *Meta-Mechano* (MM) 1-10). **(D)** UMAP plot based on the meta-analysis displaying cells of each data set by separate colors; all data sets contributed cells to each subtype. **(E)** smFISH showing that all vagal neurons are *VGlut2*+ (*Slc17a6*); they express *Prrxl1* or *Phox2b* that distinguish jugular and nodose ganglia, respectively. **(F)** smFISH showing that nodose neurons (*Phox2b*+) express *Piezo2* or *Trpv1* that mark putative mechanosensory and chemosensory neurons, respectively. **(G)** UMAP plots for *VGlut2* (*Slc17a6*), *Prrxl1*, *Phox2b*, *Trpv1* and *Piezo2*. Data in A are represented as mean ± SD. Images in **(E, F)** were stitched using the tile-scan mode.

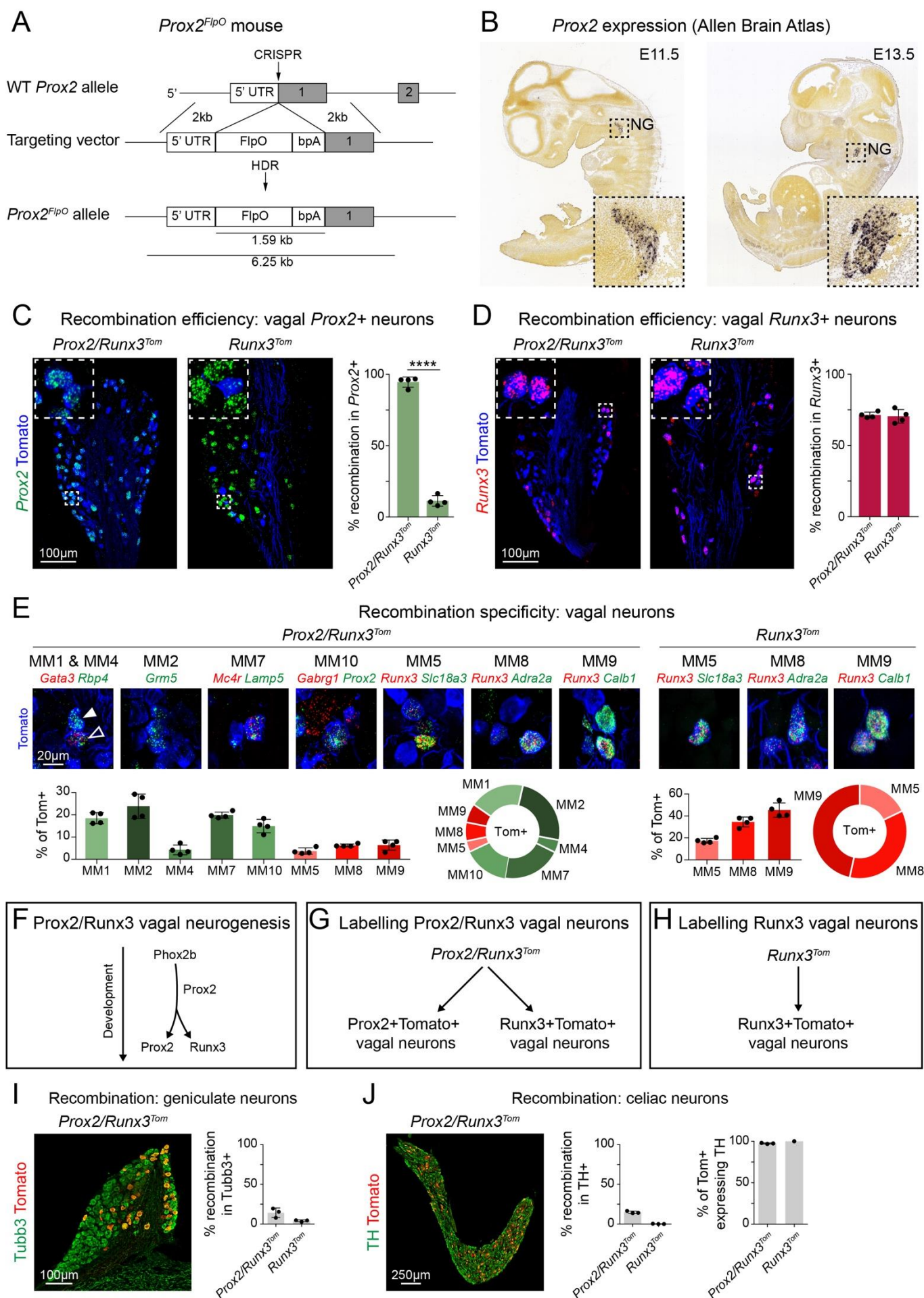


Figure S2. Generation and characterization of the *Prox2^{FlpO}* mouse strain, related to Figure 2. (A) Scheme showing the strategy used to generate the *Prox2^{FlpO}* allele. (B) *In situ* hybridizations against *Prox2* mRNA in sagittal sections of E11.5 (left) and E13.5 (right) embryos; images were obtained from the Allen Brain Atlas (<https://developingmouse.brain-map.org/>). (C) Recombination efficiency in *Prox2*⁺ neurons in *Prox2/Runx3^{Tom}* (*Prox2^{FlpO};Phox2b^{Cre};Ai65*) (left) and *Runx3^{Tom}* (*Runx3^{Cre};Prox2^{FlpO};Ai65*) (right) animals determined by smFISH analysis of *Prox2* (green) and immunohistological analysis of tdTomato expressing cells (blue). Quantifications are indicated, n=4. (D) Recombination efficiency in *Runx3*⁺ neurons in *Prox2/Runx3^{Tom}* (left) and *Runx3^{Tom}* (right) animals determined by smFISH analysis of *Runx3* (red) and immunohistological analysis of tdTomato expressing cells (blue). Quantifications are indicated below, n=4. (E) smFISH images from *Prox2/Runx3^{Tom}* (left) animals showing recombination in *Prox2*⁺ (green) and *Runx3*⁺ (red) neuronal subtypes. smFISH images from *Runx3^{Tom}* (right) animals showing recombination in *Runx3*⁺ (red) subtypes. Quantifications are indicated below, n=4. (F) Putative lineage relationships between *Prox2* and *Runx3* neurons. We propose that *Runx3*⁺ neurons have a history of *Prox2* expression and are therefore labelled in *Runx3^{Cre};Prox2^{FlpO};Ai65* mice. (G) Strategy used to label *Prox2* and *Runx3* vagal neurons with tdTomato using *Prox2/Runx3^{Tom}* (*Prox2^{FlpO};Phox2b^{Cre};Ai65*) mice. (H) Strategy used to label *Runx3* vagal neurons with tdTomato using *Runx3^{Tom}* (*Runx3^{Cre};Prox2^{FlpO};Ai65*) mice. (I) Immunohistological analysis (left) using tdTomato (red) and *Tubb3* (green) antibodies shows recombination in geniculate neurons of a *Prox2/Runx3^{Tom}* animal. Quantifications (right) of recombination in *Prox2/Runx3^{Tom}* and *Runx3^{Tom}* mice, respectively, n=3. (J) Immunohistological analysis (left) using tdTomato (red) and TH (green) antibodies shows recombination in celiac neurons of a *Prox2/Runx3^{Tom}* animal. Quantifications (right) of recombination in celiac TH⁺ neurons, and of TH expression in recombined (tdTomato⁺) neurons in *Prox2/Runx3^{Tom}* and *Runx3^{Tom}* mice, respectively, n=3. Only a third of *Runx3^{Tom}* mice showed any recombined celiac neurons, and these were all TH⁺. Data are represented as mean ± SD, ****p < 0.0001, unpaired two-tailed t-test. Images in (C, D, I, J) were stitched using the tile-scan mode.

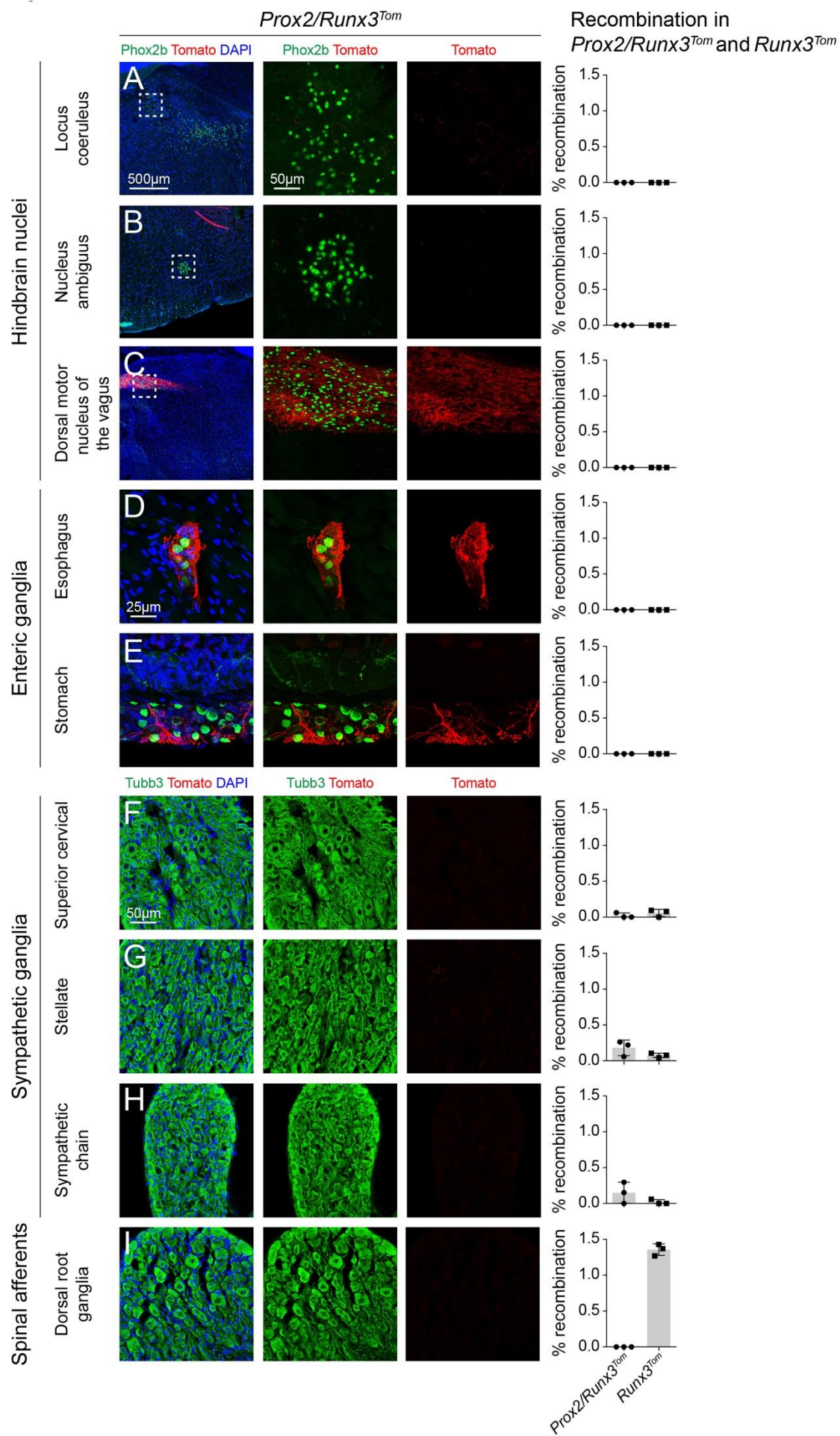


Figure S3. Recombination in *Prox2/Runx3^{Tom}* and *Runx3^{Tom}* animals, related to Figure 2. (A-E) Immunohistological analysis using antibodies against Phox2b (green) and tdTomato (red) of the **(A)** locus coeruleus, **(B)** nucleus ambiguus, **(C)** dorsal motor nucleus of the vagus, **(D)** esophageal enteric ganglia and **(E)** stomach enteric ganglia in *Prox2/Runx3^{Tom}* animals; DAPI (blue) was used as a counterstain. Quantifications **(right)** of recombination in Phox2b+ in *Prox2/Runx3^{Tom}* and *Runx3^{Tom}* mice, respectively, n=3. **(F-I)** Immunohistological analysis using antibodies against Tubb3 (green) and tdTomato (red) of the **(F)** superior cervical, **(G)** stellate, **(H)** sympathetic chain, and **(I)** dorsal root ganglia in *Prox2/Runx3^{Tom}* mice; DAPI (blue) was used as a counterstain. Quantifications **(right)** of recombination in Tubb3+ cell in *Prox2/Runx3^{Tom}* or *Runx3^{Tom}* mice n=3. Data are represented as mean \pm SD.

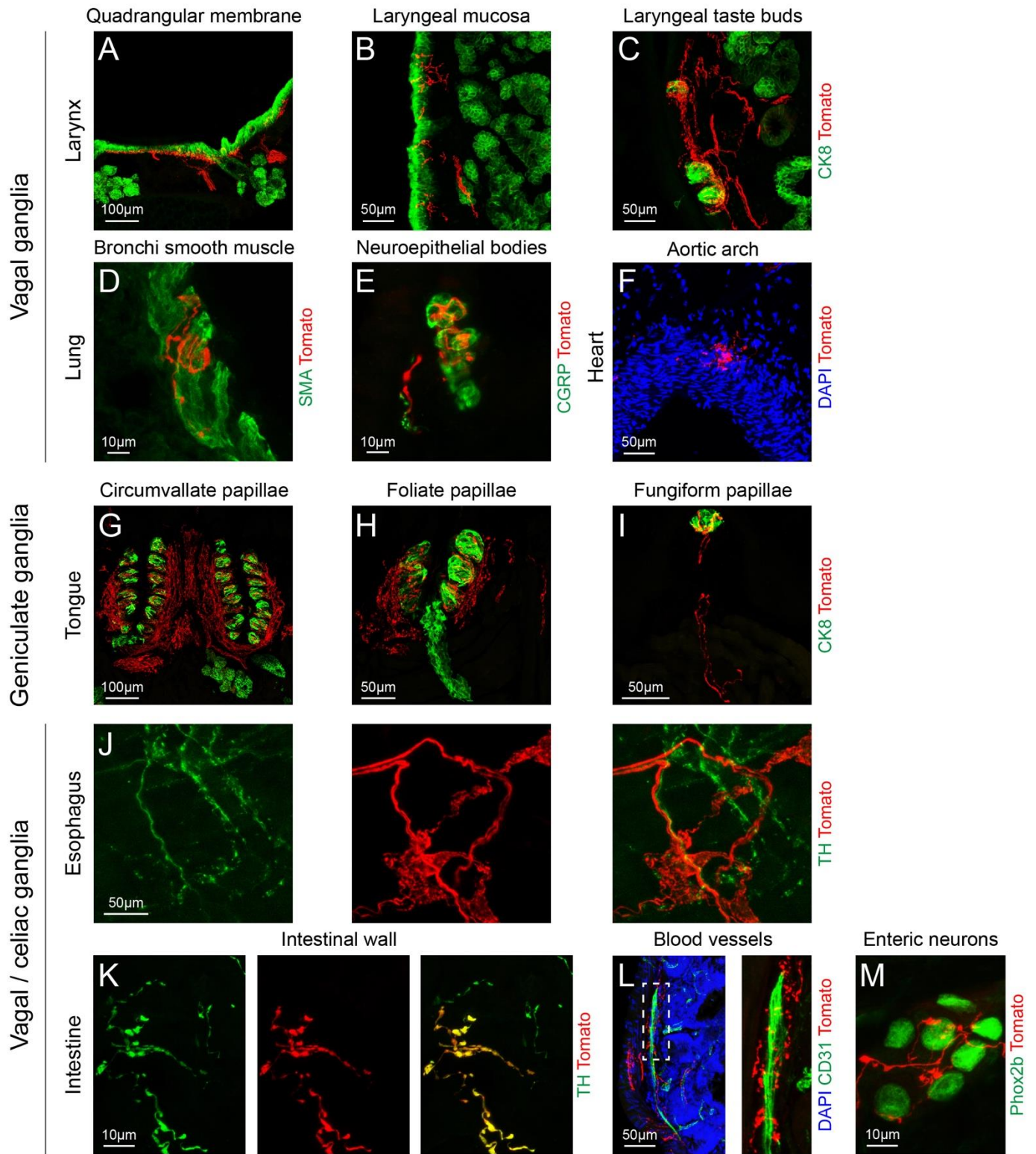


Figure S4. Innervation targets of *Prox2/Runx3* neurons, related to Figure 2. (A-C) Immunohistological analysis using Ck8 (green) and tdTomato (red) antibodies shows vagal tdTomato+ innervation of the **(A)** quadrangular membrane of the larynx, **(B)** laryngeal mucosa, and **(C)** laryngeal taste buds. **(D)** Immunohistological analysis using SMA (green) and tdTomato (red) analysis shows vagal tdTomato+ innervation of smooth muscle cells of bronchi in the lung. **(E)** Immunohistological analysis using antibodies against CGRP (green) and tdTomato (red) shows vagal tdTomato+ innervation of neuroepithelial bodies in the lung. **(F)** Immunohistological analysis using tdTomato (red) antibodies shows vagal tdTomato+ innervation of the aortic arch; DAPI (blue) was used as a counterstain. **(G-I)** Immunohistological analysis using antibodies against Ck8 (green) and tdTomato (red) shows geniculate tdTomato+ innervation of **(H)** circumvallate, **(I)** foliate, and **(J)** fungiform papillae. **(J,K)** Immunohistological analysis using antibodies against TH (green) and tdTomato (red) shows the absence of axons co-expressing TH and tdTomato in the esophagus, but extensive co-expression in the intestine. **(L)** Immunohistological analysis using antibodies against CD31 (green) and tdTomato (red) shows endings on blood vessels in the intestine. **(M)** Immunohistological analysis using antibodies against Phox2b (green) and tdTomato (red) shows varicose endings on enteric ganglia in the intestine. Images in (A, G, H, J, K, L) were stitched using the tile-scan mode.

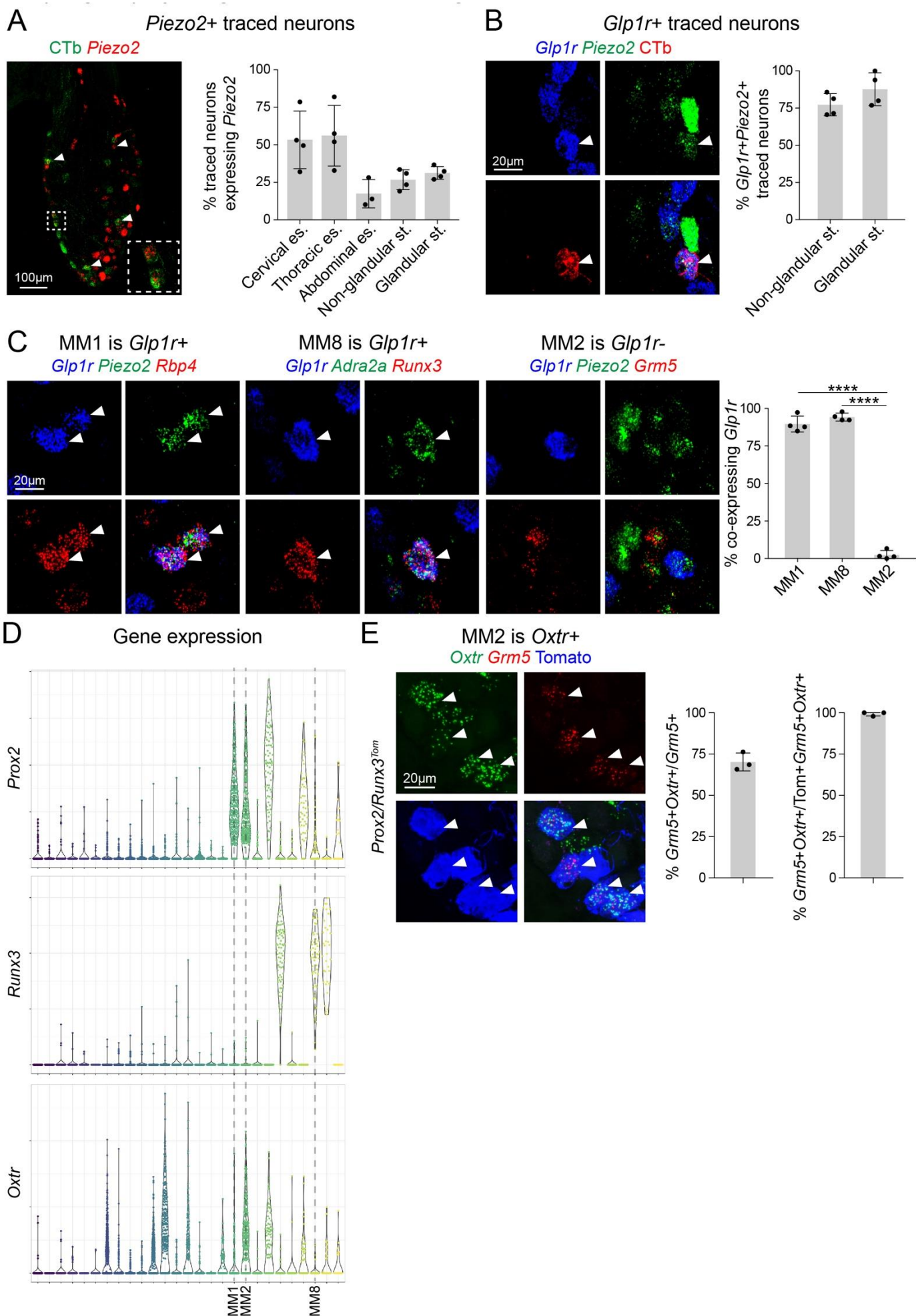


Figure S5. MM1 and MM8 include *Glp1r*+ stomach projecting neurons, MM2 include *Oxtr*+ esophageal projecting neurons, related to Figure 3. (A) smFISH (left) analysis of the vagal ganglion using a *Piezo2* (red) probe, combined with an immunohistological analysis of CTb (green) after CTb injection into the glandular stomach. (Right) Quantification of *Piezo2*+ neurons identified after CTb or Fast Blue injection into various sites of the upper gastrointestinal tract, n=3–4. Neurons from the cervical and thoracic esophagus were traced using Fast Blue at P7, and neurons from the abdominal esophagus, non-glandular and glandular stomach were traced using CTb in adults. (B) smFISH analysis of the vagal ganglion (left) using *Piezo2* (green) and *Glp1r* (blue) probes, combined with immunohistological analysis of CTb (red) after CTb injection into the stomach. The quantification after injection into the glandular and non-glandular is shown on the right; n=4. (C) smFISH analysis (left) of *Glp1r* expression in MM1 (probes: *Piezo2* in green, *Rbp4* in red, and *Glp1r* in blue, left), MM8 (probes: *Adra2a* in green, *Runx3* in red, and *Glp1r* in blue, middle) and MM2 (probes: *Piezo2* in green, *Grm5* in red, and *Glp1r* in blue. The quantification of the proportions of MM1, MM8 and MM2 neurons expressing *Glp1r* is shown on the right, n=4. (D) Violin plots for *Prox2*, *Runx3* and *Oxtr* expression derived from the meta-analysis. MM1, MM2 and MM8 subtypes are indicated. (E) smFISH analysis using (left) of *Oxtr* (green) and *Grm5* (red) probes, combined with immunohistological analysis using tdTomato antibodies (blue). Among the *Prox2*/*Runx3* neuronal subtypes, only MM2 expresses *Grm5*. The quantifications of MM2 neurons (*Grm5*+) expressing *Oxtr*, and of recombined *Oxtr*+ MM2 (*Grm5*+) neurons (i.e. tdTomato+) in *Prox2*/*Runx3*^{Tom} animals is shown on the right, n=3. Data are represented as mean \pm SD, **p < 0.0001, unpaired two-tailed t-test (B), Ordinary one-way ANOVA with Tukey's multiple comparisons test (C). Image in (A) was stitched using the tile-scan mode.**

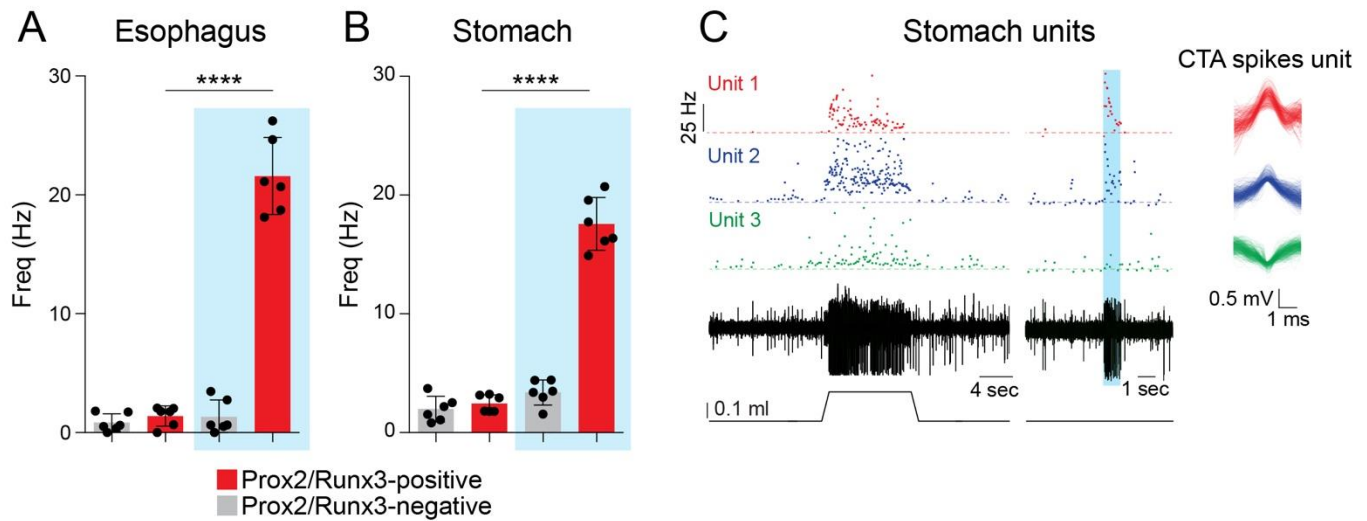


Figure S6. Optogenetic activation of Prox2/Runx3 mechanoreceptors, related to Figure 4. **(A,B)** Quantification of the firing properties of Prox2/Runx3-positive (red, light-sensitive) and Prox2/Runx3-negative (gray, light-insensitive) single fibers. Action potential firing frequency (Hz) was measured on single esophageal **(A)** or stomach **(B)** fibers from *Prox2/Runx3^{ChR}* (*Prox2^{FlpO};Phox2b^{Cre};Ai80*) animals with and without blue light stimulation (indicated in blue shading). Under light stimulation, Prox2/Runx3-positive units dramatically increased their firing frequency; $n=6$. **(C)** Spike sorting identified three individual mechanosensitive units (shown in red, blue and green) present in a single fiber. Points form a raster plot of single unit instantaneous firing frequencies after stomach distention (**left**, 0.3 ml stimuli, the black line underneath the plot displays the change in stomach volume), or light activation (indicated by blue shading). Note that units 1 and 2 (red and blue) are light-sensitive and thus Prox2/Runx3-positive, whereas the light insensitive unit 3 (green) is Prox2/Runx3-negative. Cycle trigger average (CTA) of 500 spikes (**right**) of the 3 units identified in this fiber after stomach distention. Data are represented as mean \pm SD, **** $p < 0.0001$, Ordinary one-way ANOVA with Tukey's multiple comparisons test.

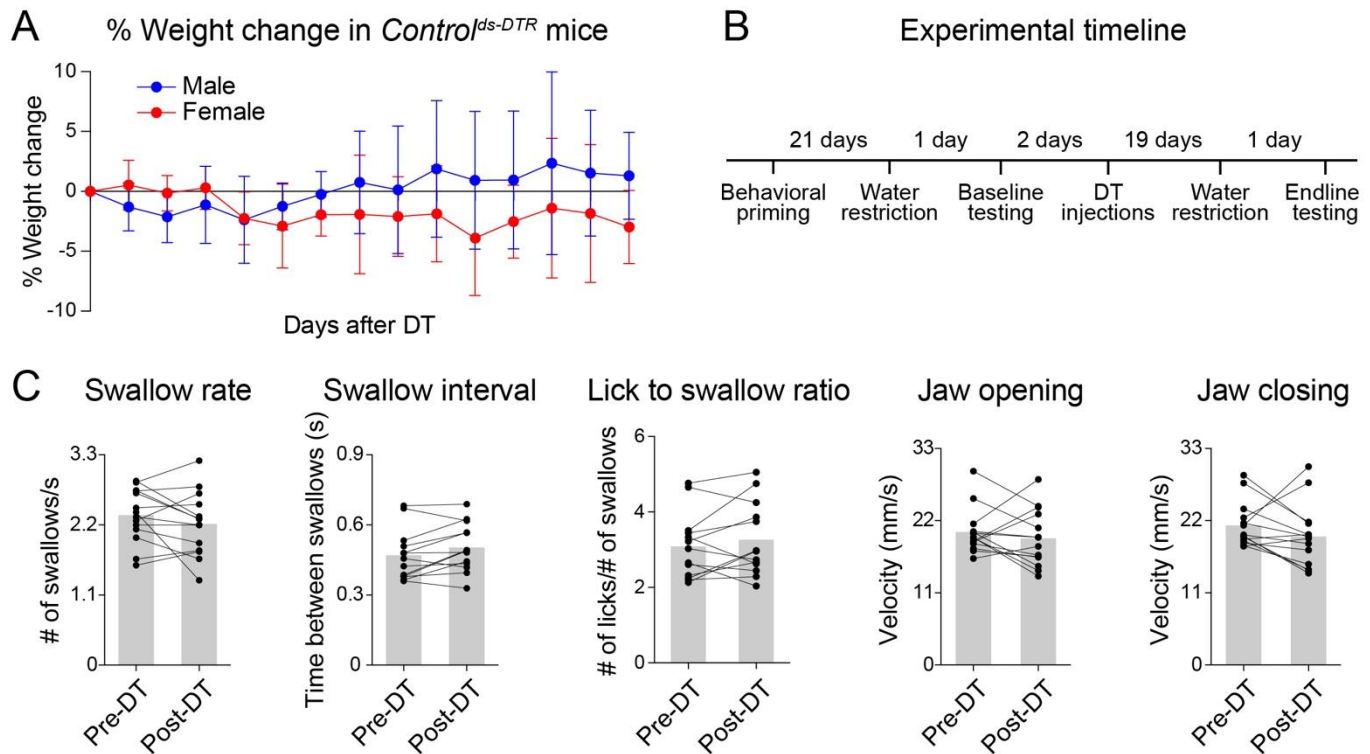


Figure S7. Oropharyngeal swallow-related behaviors that were not affected by ablation of Prox2/Runx3 neurons, related to Figure 5. (A) Graph showing weight change in *Control*^{ds-DTR} (*Prox2*^{FlpO}; *Tau*^{ds-DTR}) control mice over 14 days after DT administration. **(B)** Outline of the experimental timeline. **(C)** Many oropharyngeal swallow-related behaviors were not affected after ablation of Prox2/Runx3 neurons. Swallow rate, swallow interval, lick to swallow ratio, jaw opening and closing velocity were unaffected, n=13-14. Data are represented as mean \pm SD, paired two-tailed t-test.